Experimental Study of Mean Flow Characteristics over a Low Speed All-Body Lifting Aeroplane
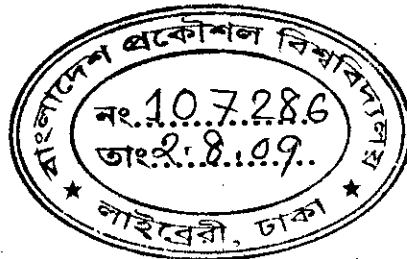
By

Md. Moinul Islam Forhad

A thesis

Submitted to the

Department of Mechanical Engineering

in partial fulfillment of the requirements for the degree

of

MASTER OF SCIENCE IN MECHANICAL ENGINEERING

নং.১০.৭.২৮.৬
তাং.২..৮.০৯..

BANGLADESH UNIVERSITY OF ENGINEERING AND TECHNOLOGY
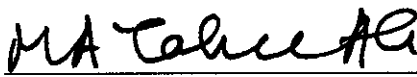
DHAKA

August 2009

The thesis titled **"Experimental Study of Mean Flow Characteristics over a Low Speed All-Body Lifting Aeroplane"** submitted by **Md. Moinul Islam Forhad,** Roll no. 040810044 F, Session April 2008 has been accepted as satisfactory in partial fulfillment of the requirement for the degree of Master of Science in Mechanical Engineering on August 16, 2009.
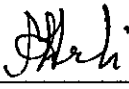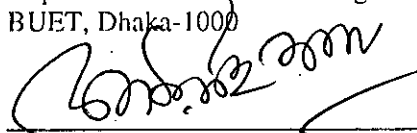
BOARD OF EXAMINERS

1. _____

   Dr. M. A. Taher Ali   Chairman
   Professor
   Department of Mechanical Engineering
   BUET, Dhaka-1000

2. _____

   Dr. Abu Rayhan Md. Ali   Member (Ex-Officio)
   Professor and Head
   Department of Mechanical Engineering
   BUET, Dhaka-1000

3. _____

   Dr. Mohammad Ali   Member
   Professor
   Department of Mechanical Engineering
   BUET, Dhaka-1000

4. _____

   Dr. Mohammad Mamun   Member
   Associate Professor
   Department of Mechanical Engineering
   BUET, Dhaka-1000

5. _____

   Dr. A.K.M. Sadrul Islam   Member (External)
   Professor, MCE Department, IUT,
   Board Bazar, Gazipur

CANDIDATE'S DECLARATION

It is hereby declared that this thesis or any part of it has not been submitted elsewhere for the award of any degree or diploma.

Md. Moinul Islam Forhad

To my Parents

ACKNOWLEDGEMENT

ABSTRACT

The mean flow characteristics over an all-body lifting aeroplane are investigated in the speed range of 30 km/hr to 40 km/hr. The aim is to study the nature of boundary layer and boundary layer separation and wake formation. A model with NACA 2412 aerofoil in both the fuselage and the wings is made with a better aerodynamics shape following the design of MIG-29 fighter plane. From the investigations carried out at an angle of attack of 4°, it is found that in the case of 30 km/hr speed over the wing, separation starts at nearly 25% of chord length and continues till 60% of the chord length while for 40 km/hr speed over the wing, it starts at the same point but the zone of separation shrinks to certain extent and the boundary layer reattaches at 50% of the chord length. In case of the fuselage both the starting point of separation and the reattachment point shift backward while the span of separation zone remains almost the same, for both the speeds. It is found that the length of separation zone reduces at the curved section of the wing as compared to that at the center of the wing, for both speeds. Velocity profiles on the lower surfaces of both the fuselage and the wings are measured along with the flow angles and no separation was found on any of the lower surface. However, near the trailing edge of both the fuselage and the wing, there are evidences of wake formation. The vector diagrams present a complete picture of the flow filed.

TABLE OF CONTENTS

CHAPTER 3
ABOUT THE MODELS

CHAPTER 4
EXPERIMENTAL SETUP

CHAPTER 5
EXPERIMENTAL PROCEDURE

CHAPTER 6
RESULTS AND DISCUSSION

CHAPTER 7

CONCLUSIONS AND RECOMMENDATIONS

LIST OF FIGURES

LIST OF TABLES

LIST OF SYMBOLS

Symbols	Meaning	Unit
Re	Reynolds number	--
U	Local velocity	m/s
U_∞	Free stream velocity	m/s
δ	Boundary layer thickness	mm
δ_l	Displacement thickness	mm
V	Relative velocity between the wing and air	km/hr
C_L	Lift coefficient	--
C_D	Drag coefficient	--
C_M	Moment coefficient	--
C_P	Pressure coefficient	--
S_{ref}	Area of the wing when viewed from the overhead	m^2
C	Chord length	mm
b	Span	mm
AR	Aspect ratio	--
ρ	Air density	Kg/m^3
g	Gravitational acceleration	m/s^2
h	Manometric column	mm
x	Stream wise distance from the front of the fuselage	mm
y	Vertical distance	mm
Θf	Fuselage angle of attack in degree	degree
Θw	Relative angle between wing and fuselage	degree
L	Lift force	kg
D	Drag force	kg
L/D	Lift to Drag ratio	--
βi	Angle between cord and pressure taps direction	degree
α	Angle of attack of the pressure taped fuselage	degree
θ	Flow angle relative with horizontal plane	degree
l_i	Corresponding length represent by a single tap	mm
ν	Kinematic viscosity	m^2/s

Chapter 1

INTRODUCTION
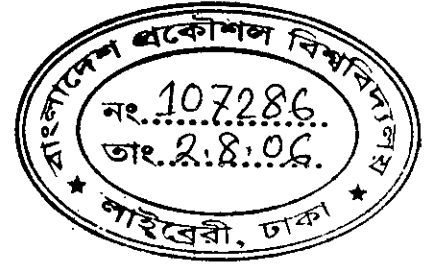
1.1. Preamble

Wide body transport aircraft or unmanned aerial vehicle (UAV), increased lift along with low drag has always been the major thrust in designing of aircrafts. Early research works to develop the most efficient aerofoil section that would produce the maximum lift corresponding to relatively small drag, dates back to the beginning of 20th century. For different airfoil profiles, coefficient of lift (C_L) and that of drag (C_D) have been measured or calculated. In conventional airplanes, aerofoil sections are used as the wings, which ultimately produces more than 90 percent lift while in some cases the total 100 percent. In these airplanes, fuselage has little or no contribution in production of lift while adding a substantial portion of total drag. To obtain a good overall lift to drag ratio, the total drag produced by each exposed parts of the airplane needs to be minimum and hence, designing of an airplane should include reduction of the drag forces on exposed parts. In addition to minimizing drag forces, an enhanced lift produced by ensuring some lift from each of the exposed parts can be an intelligent way of maximizing the overall lift to drag ratio.

So in order to maximize the efficiency of an aircraft, the basic design premises should be such that all elements/components of the aircraft must contribute to the aircraft lift. In pursuit of this goal and to solve the present challenges and future goals of the air transportation system of increased efficiency, passenger safety and productivity combined with greater personal mobility and expanded transportation capability, the scientific community is now turning there attention to the lifting-body aircraft. The lifting-body aircraft design principle allows the designer both safe and fuel-efficient aircraft for an efficient utilization of the air transportation system for the movement of people and goods. This design would also provide increased payload and a dramatically improved short take-off and landing (STOL) capability, over conventionally designed [1-5] aircraft. In conventional designs, the aircraft fuselages are generally circular and the wings have aerofoil sections. Despite the advantage of less drag in a circular fuselage, it has limitations that it produces no lift. The fuselage of the aircraft, when the conventional circular

i

section is replaced by an aerofoiled section, is expected to increase overall lift to drag ratio by producing an additional lift on the fuselage surfaces. The airplane with aerofoiled section fuselage is termed as all body lifting aircraft.

1.2. Background of the Work on Aerofoiled Fuselage

In early 20th century a famous professional aircraft designer Vincent Justus Burnelli [6] developed the concept of all body lifting aircraft where he used fuselages of aerofoil cross section. But this fuselage aerofoil section had to be sufficiently thick such that man could ride on it. So the scientific community had raised a number of technical concerns related to the large fuselage and its impact on aerodynamics. Amongst these primary concerns was the negative aerodynamic drag effects attributed to the lifting-body fuselage due the increased fuselage frontal area and the fuselage wing interference. Figure 1.1 shows the Burnelli's designed first aerofoiled section fuselage bi-plane [6]. The bi-plane was very large, capable of carrying 26 passengers. Figure 1.2 shows Brunelli's another lifting fuselage aircraft designed in 1927.
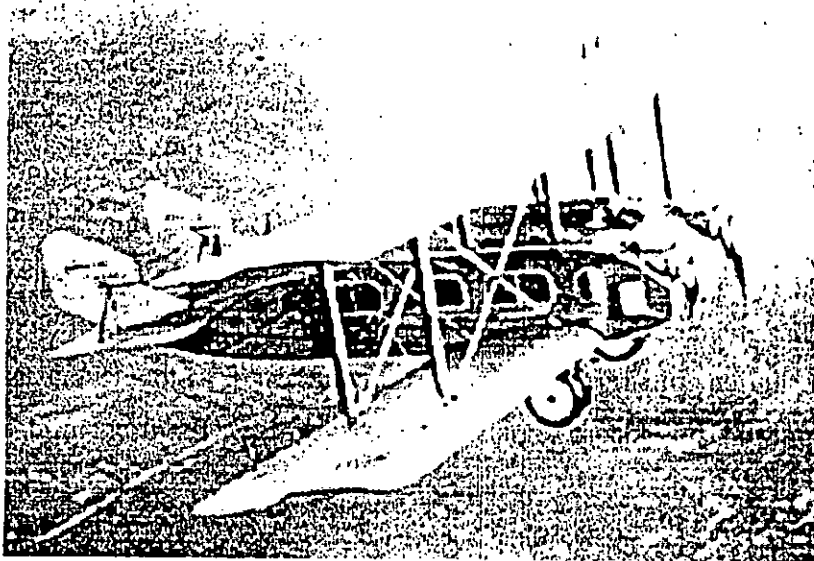
Figure 1.1: Burnelli's all body lifting fuselage bi-plane, RB-1, designed in 1921.

Figure 1.2: Burneeli's CB-16 airplane in flight with landing gear retracted.

An analysis of the concept performed by Wertenson [7, 8] in 1931 showed that the Burnelli's design concept resulted in less frontal area than a conventional twin-engine transport airplane and that the negative fuselage wing interference is more than compensated by the increased lift of the fuselage. But Burnelli himself did not study the flow characteristics of his invented airplane Subsequent analysis performed at that time by some researchers [9-12] also supported the findings of Wertenson.

Now-a-days Unmanned Aerial Vehicles are being extensively used in various applications with a view, mainly, to reducing risk to human life. Besides, the idea of lowering the operational costs have always been one of the major justifications for using UAVs. As some of the UAV for area reconnaissance or similar purposes have to operate at low speeds, the present investigation is carried out in the speed range of 30 km/hr to 40 km/hr. Besides, the design present in the nature can be followed and the practical aspects of streamline form be studied from the bodies of fishes and birds, the profiles of which have gradually met the requirements of least resistance for motion through a fluid, water or air, as the case may be [16]. In this context the gliding bird's body shape could be a good natural example for a UAV design and for most of the gliding birds like Harris' hawk (Parabuteo unicinctus) have aerofoil body shape rather than conventional cylindrical shape [17]. Picture 1.3 shows the body shape of a Harris' hawk during flying condition and an UAV designed following the body shape of the bird.

Figure 1.3: All body lifting shape of a Harris' hawk (Parabuteo unicinctus)

V. A. Tuckerm.[17] made an extensive research on the lift drag characteristics on wings creating the similar conditions of birds' wings. He found that a wing that produces lift leaves a pair of vortex sheets in its wake which generates the induced drags. The feathers at the wing tips of most birds that soar over land separate both horizontally and vertically in flight to form slotted tips i.e. the winglets and the wing theory shows that winglets can reduce the kinetic energy left in the vortex sheets, and hence the induced drag, by spreading vorticity both horizontally and vertically. He also found that the total drag of the wing with the feathered tip was 12% less than that of a hypothetical wing with the same lift and span, but with tip feathers that did not respond to upwash at the end of the base wing. This value is consistent with wing theory predictions on drag reduction from winglets and the Wings with the tip and the base wing locked together had lift and drag that increased with increasing base wing angle of attack, as expected for conventional wings without winglets. [18, 19, 20, 21, 22, 23, 24].

Issac W. Newton [62] measured the separation point over NACA 2412 at varying angles of attack (AOA) and two Reynold's no. with varying test section width. He used surface oil patterns to distinguish and reveal the 3D aspect of separation at two AOAs at identical Reynold's no. He found that separation point moves forward with an increase in AOA. Increase in Reynold's no causes the separation location to move. He also concluded that separation points of an airfoil are unique.

A. Schmid and C. Breitsamter [63] measured turbulent flow-field above the wing of a delta—canard—configuration at moderate ($\alpha = 15°$) and high ($\alpha = 24°$) angle of attack at a Re—number of 0.97.106 in a wind tunnel by hotwire anemometry. Leading edge flap settings of $\eta_{l.e.} = 0°$ and $\eta_{l.e.} = -20°$ were used. He found that at moderate angle of attack and deflected leading edge flap a strong vortex originates from the side edge of the non-deflected inboard wing leading edge part. This inboard wing vortex is located close to the fuselage. It is a dominant flow feature and forms the center of the vortical flow separating from the wing surface. The separation line is clearly different from the leading edge flap hinge line. At high angle of attack the flow separates at the leading edge for both the non—deflected and deflected leading edge ease. The resulting leading edge vortex is subject to breakdown dose to the apex. In case of the deflected leading edge, the interaction of inboard wing vortex and leading edge vortex remits in decreased downstream expansion of the burst vortex, also reducing turbulence intensity levels.

Eastman N. Jacobs and Albert Sherman [25] tests of wing-fuselage combinations employing an aerofoil-type fuselage were made in the variable-density wind tunnel as a part of the wing-fuselage interference program and the test results showed that the aerofoil-type-fuselage combination should be well faired in such a way as to eliminate the discontinuity at the ends of the fuselage. The results show that the fuselage part of the lifting surface, comprising 33 percent of the total lifting area (exposed wing area plus fuselage area) contributes 26 percent of the total lift.

Kroo [26] from Stanford University, USA recently done some research work aiming to increase the commercial aircraft efficiency. His findings shows that the vortex drag of commercial aircraft accounts for a large fraction of airplane cruise drag (typically about 40%) and therefore concepts that result in reduction of vortex drag may have a significant effect on fuel consumption. Vortex drag is even more significant at low speeds where vortex drag typically accounts for 80%-90% of the aircraft's climb drag at critical take-off conditions [26]. Although take-off constitutes a very small portion of the flight, but its influence on the overall aircraft design is profound. Since conditions associated with engine-out climb shortly after take-off are often critical constraints in the aircraft design, changes in aircraft performance at these conditions influence the overall

design and so have an indirect, but powerful, effect on the aircraft cruise performance. While a 1% reduction in drag due to lift might improve the cruise lift-to-drag ratio by 0.4% with a similar effect on range, the improved low speed climb performance may make it possible to achieve acceptable take-off and climb with almost 1% greater take-off weight, leading to an increase in range several times that associated with the simple cruise L/D improvement [26, 27]. Furthermore, lower drag at high lift conditions leads to reduced noise. He also noted that the induced drag may be easily reduced by increasing the span of a planar wing. A 10% increase in wing span leads to a 17% reduction in vortex drag at fixed speed and lift [26]. But the primary reason that wing spans are not increased to reduce drag is that the higher structural weight and cost make such efforts counterproductive. To produce a large change in the vortex drag without a large increase in wetted area, his low aspect ratio endplates were replaced with higher aspect ratio winglets.

Nay, Harvey O. [64] at California Institute of Technology, USA performed conducted Low-speed tests to determine boundary layer and surface pressure distribution characteristics of a systematic family of swept back wings, with a view to making a better understanding of the viscous flow phenomena on swept back wings, particularly in relation to the stall with the help of test results. He determined a general picture of the boundary layer flow and surface pressure distribution at high lift conditions, showing the effects of variations in wing planform. Several existing concepts were verified and an attempt was made to define the limits of applicability of these concepts. He found a localized separation of the flow perpendicular to the leading edge of the wing, which he referred to as the "normal flow", that occur at lift coefficients somewhat below the stall on the wings with appreciable sweepback. The separation took the form of a vortex streak running aft and outboard from an origin near the leading edge, and it greatly affected the boundary layer structure and the surface pressure distribution. He also found that generalization of surface pressure distribution on the basis of the local lift coefficient and dynamic pressure for the normal flow holds fairly well for the various sweepback angles. In addition, he determined the development of stall for the various planforms in terms of boundary layer thickness and flow direction near the surface of the wing. He concluded that generalization of the shape of the profiles of the normal boundary layer flow component in terms of a single family of shapes for all sweep-back angles, as suggested by other researchers, was possible.

Hahl, Robert W. (Falls Church, VA) [61] studied a lifting-fuselage/wing aircraft having low drag at a selected cruise condition. The aircraft included (a) a lifting fuselage having a cross-section constituting an airfoil in a majority of vertical planes taken parallel to the flight direction and an aspect ratio of 0.33 to 1.10; (b) wings fixed to the fuselage having an aspect ratio of at least 5.0; (c) a mechanism controlling aircraft attitude; and (d) a mechanism propelling the aircraft; wherein the wings and fuselage produce lift in varying proportions depending upon flight conditions as follows: (i) the aircraft had a cruise design point in which the fuselage lift coefficient was 0.08 or less, and (ii) the fuselage lift coefficient was at least 0.50 at an angle of attack of 10°, in level flight at sea level (ISA) with all movable lift enhancing devices retracted. Figure 1.4 shows the model investigated by Hahl.
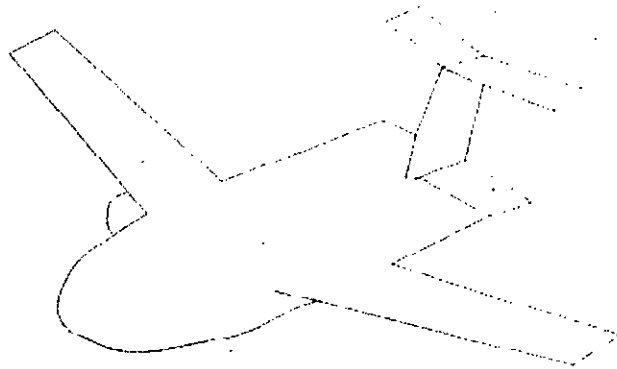
Figure 1.4: Model investigated by Hahl

Hahl calculated the fuselage lift coefficient (C_{LF}) of his invention by measuring total fuselage lift (with flaps and the like retracted and attributing carryover lift to the fuselage) at a given calibrated airspeed and standard altitude, and applying the general formula using (S_f) as the reference area. The wing lift coefficient (C_{Lv}) of his model was calculated by measuring total wing lift (again with flaps not deployed and attributing carryover lift to the fuselage only), and applying the general formula using (S_w) as the reference area. The quantity (C_{Lv}) is therefore different from the more common definition of lift coefficient which is based upon a wing reference area including part of the fuselage between the wings.

At the design cruise condition, Hahl found that C_{LW}/C_{LF} is greater than 4 and generally between 8 and 1000, preferably 10 to 100. At minimum calibrated airspeed in level flight at sea level ISA, C_{LW}/C_{LF} is generally 0 to 4.0, preferably 0.5 to 3.0. Hahl concluded that variations of his invention are possible in light of the above findings.

To increase the maneuvering capability of the modern fighter plane it's also utilized the all body lifting fuselage concept. For example from Bill Gunston's excellent encyclopedia (page 224), the modern fighter jet MiG-29 has high maneuvering capability as it's design specifics are defined for 40% aerodynamic lift from the central structure component comprising fuselage and inner wing between fins. This type of fighter plane is called Blended Wing Body (BWB) aircraft. For a better understanding of the BWB shape visually and practically a recent visit to Bangladesh Air Force (BAF) has been arranged by Mechanical Department, BUET under the guidance of Professor Dr. M. A Taher Ali. The BAF engineers, pilots and the officers extensively describe different parts, body shape and their aerodynamic function by dismantling a BAF owned MIG-29 fighter plane. The visit helps this research works to understand the practical advantage of lifting body fuselage. Picture 1.5 is showing the Blended Wing Body (BWB) outer shape of a MIG-29 fighter plane.
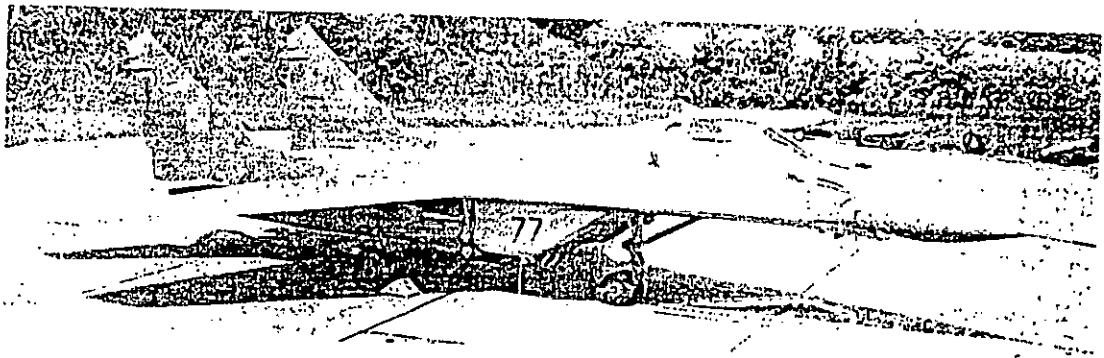
Figure 1.5: Photograph of a MIG-29 showing lifting body fuselage
(Source: http://commons.wikimedia.org/wiki/File:060610-SKP-MIG-29-01-1280x.jpg)

1.3. Overview of the present work

For any design, the aerodynamic performance of an aircraft is totally dependent on the flow characteristics over the airplane. Hence, this investigation is carried out with a view to seeing the nature of boundary layer and its effects on lift and drag, and understanding the effect of interference on the nature of boundary layer and wake formation.

Particular objectives of this research include:

(a)   To find the direction of flow over the aerofoil fuselage and the wings and hence obtain the velocity profile over the top and bottom surfaces of both fuselages in the longitudinal direction at different angles of attack.

(b)   To investigate the characteristics of the overall lift to drag ratio of aerofoil cross-section fuselages in the speed range of 50-100 km/hr at different angles of attack and compare them with those of conventional fuselages with the help of available data.

(c)   To compare the results of lift and drag forces obtained from both of the above measurement methods and to determine the difference between them.

(d)   To calculate the take off and landing speeds hence determining flight safety.

In this research work, the direction of flow over the aerofoil fuselage and the wings is measured and hence the velocity profiles over the top and bottom surfaces of both the wing and the fuselage in the longitudinal direction is found out and drawn for an angle of attack of 4°.

At the very beginning of this work, the previous model of Mainuddin [ ] is extensively modified with a view to obtaining a more efficient aerodynamic shape. While making this modification, the design of MIG-29 fighter plane is taken as a guide.

In this experimental study, yawmeter is used to find the velocity profiles and direction of flow over the surfaces and hence study any formation of wakes. Effects of formation of wakes on the performance is later investigated and anlaysed. The result of this investigation provides with information about the flow characteristics around the aeroplane and it is expected that this wi'l help in designing the all body lifting aircraft in future.

9

Chapter 2

THEORETICAL CONSIDERATION

Aerodynamics is nothing more than the study and application of those natural laws that influence flight. Some of these laws are well defined and well understood, whereas others are obscure and their presence is just beginning to be suspected. Airplane design progress is directly dependent on our advances in understanding the aerodynamics laws. Some of the theoretical consideration and the aerodynamics laws are discussed below.

As an object moves through a fluid, or as a fluid moves past an object, the molecules of the fluid near the object are disturbed and move around the object. Aerodynamic forces are generated between the fluid and the object. The magnitude of these forces depend on the shape of the object, the speed of the object, the mass of the fluid going by the object and on two other important properties of the fluid; the viscosity, or stickiness, and the compressibility, or springiness, of the fluid. To properly model these effects, aerospace engineers use similarity parameters which are ratios of these effects to other forces present in the problem. If two experiments have the same values for the similarity parameters, then the relative importance of the forces are being correctly modeled.

Aerodynamic forces depend in a complex way on the viscosity of the fluid. As the fluid moves past the object, the molecules right next to the surface stick to the surface. The molecules just above the surface are slowed down in their collisions with the molecules sticking to the surface. These molecules in turn slow down the flow just above them. The farther one moves away from the surface, the fewer the collisions affected by the object surface. This creates a thin layer of fluid near the surface in which the velocity changes from zero at the surface to the free stream value away from the surface. Engineers call this layer the boundary layer because it occurs on the boundary of the fluid.

To be successful an aircraft must be capable of doing the job it is designed for, economically and easily. In addition to fulfilling other requirements concerning structural adequacy, safety systems, stability, take off and landing, the air craft must have an adequate system for producing lift or sustention. An aircraft deficient in respect to any one of the key requirements cannot be considered satisfactory, regardless of how well it meets all the others. It is difficult in one design to meet perfectly all of the above requirements for a successful airplane. The designer must be satisfied with excellence in as many as characteristics as possible and adequate in the remainder. The designer must exercise his best judgment in deciding what requirements may be considered of secondary importance without jeopardizing the airplane utility.

The details of the flow within the boundary layer are very important for many problems in aerodynamics, including wing stall, the skin friction drag on an object, and the heat transfer that occurs in high speed flight. Irrespective of shape, structural features, powerplant efficiency, safety and utility systems, any other design criteria, the aerodynamic performance of an aircraft is ultimately dependent on the flow characteristics over the airplane. Understanding of flow characteristics on the airplane requires investigation of the nature of boundary layer and its effects on lift and drag, and understanding the effect of interference on the nature of boundary layer and wake formation. Since, flow separation is an unavoidable phenomenon in case of real fluid flows, an efficient design of an aircraft also necessitates thorough understanding of boundary layer separation in the design regime of flow.

2.1 Boundary Layer

A boundary layer is a thin region of fluid near a wall where viscous effects are important in determining the flow field. The boundary layer is a buffer region between the wall below and the inviscid free-stream above. The layer of air extending from the surface of the object to the point where no dragging effect is discernible is known as the boundary layer. Mathematically, its main purpose is to allow an inviscid flow solution to satisfy the no-slip condition at the wall.
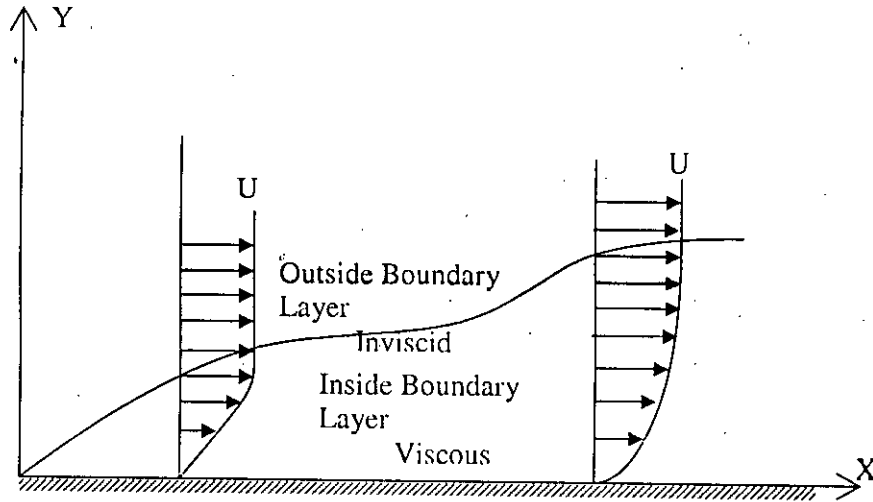
Figure 2.1: Boundary layer formation

Figure 2.1 shows the growth of boundary layer. Conventionally, the X-axis is parallel to the wall, while the Y-axis is perpendicular to the wall and cuts right through the boundary layer. At any given x-coordinate, we can draw the velocity distribution as a function of y. This is the most common way to illustrate a boundary layer. Figure 2.1 also shows velocity cross sections of two points in the boundary layer. The first is the cross section for a laminar boundary layer; the second one is after the transition and represents a turbulent boundary layer. It should be noted that, in a boundary layer, the velocity is always zero at the wall, and asymptotically approaches the free-steam velocity (denoted by U_∞) at infinity. The boundary layer typically grows in thickness in the stream-wise direction. Turbulent boundary layers grow faster than laminar ones.

The nature of the boundary layer is a controlling factor in the determination of skin-friction drag. More important than this, the nature of the boundary layer determines maximum lift coefficient,

stalling characteristics of a wing and, magnitude of the friction and pressure drag and to some extent the high speed characteristics of any object.

2.2 Laminar and Turbulent Boundary Layers:

There are two different types of real fluid flow: laminar and turbulent. In laminar flow the fluid moves in layers called laminas. In turbulent flow, secondary random motions are superimposed on the principal flow.
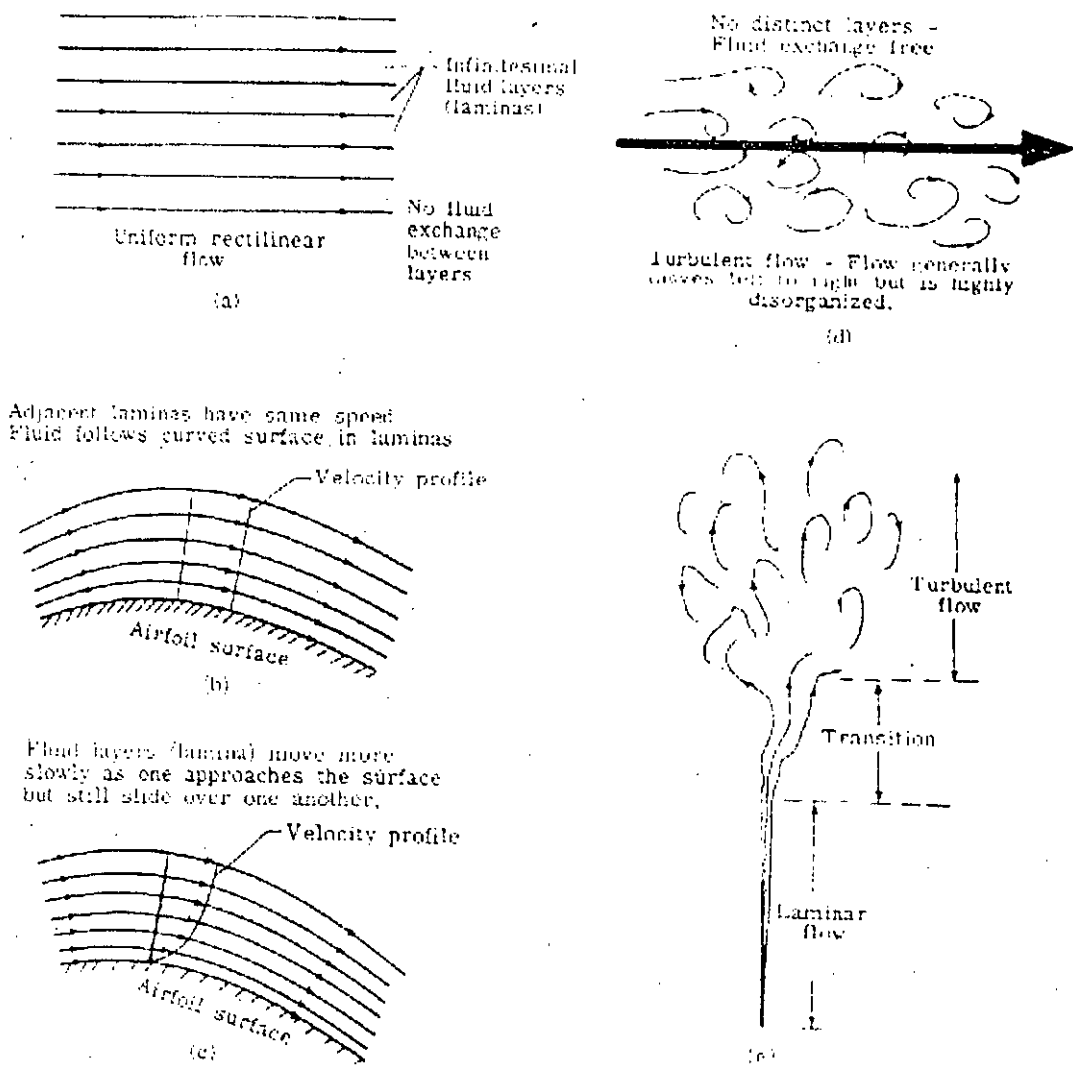
Figure- 2.2: Laminar and Turbulent Boundary Layer

The laminas may be considered the adjacent streamtubes and then the streamlines indicate the direction of movement of these fluid layers. The upper one of firgure 2.2 (a) shows a laminar flow, the uniform rectilinear flow, consisting of air moving in straight-line layers (laminas) from left to right. The laminas may be considered the adjacent streamtubes and then the streamlines indicate the direction of movement of these fluid layers. Laminar flow need not be in a straight line. Figure 2.2 (b) shows a laminar flow, over a small segment of curved portion of an aerofoil.

In turbulent flow, secondary random motions are superimposed on the principal flow. Figure 2.2(d) shows a disorganized number of streamlines. They are evidently not fluid layers and there is an exchange of fluid from one adjacent sector to another. More importantly, there is an exchange of momentum such that slow moving fluid particles speed up and fast moving particles give up their momentum to the slower moving particles and slow down themselves. Consider figure 2.2(e) which shows the smoke rising from a cigarette. For some distance the smoke rises in smooth filaments which may wave around but do not lose their identity; this flow is laminar. The filaments (or streamtubes) suddenly break up into a confused eddying motion some distance above the cigarette; this flow is turbulent. The transition between laminar and turbulent flow moves closer to the cigarette when the air in the room is disturbed.

An example of a common occurrence of laminar and turbulent flow is the water faucet. Opened slightly, at low speeds the water flows out in a clear column - laminar flow. But open the faucet fully and the flow speeds out in a cloudy turbulent column. In a mountain brook the water may slide over smooth rocks in laminas. In the Colorado River the flow churns downstream in the confused turbulent rapids. It will be seen that the flow over airfoil surfaces may assume both a laminar and turbulent characteristic depending upon a number of factors.

In some cases, turbulent flow will appear "naturally" in a laminar flow as in the smoke rising in the air. In other cases, by causing a disturbance, a laminar flow can be changed to a turbulent flow. The question arises as to how one can tell whether a flow is to be laminar or turbulent. In 1883, Osborne Reynolds introduced a dimensionless parameter which gave a quantitative indication of the laminar to turbulent transition.

Boundary Layer
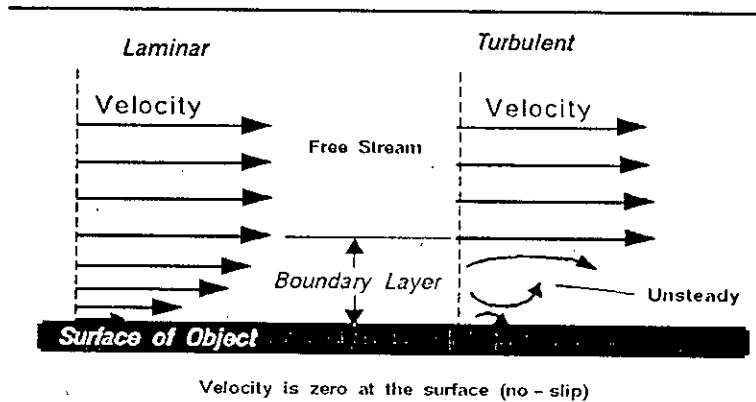
Figure- 2.3: Laminar and Turbulent Boundary Layer

Figure-2.3 shows the stream-wise velocity variation from free stream to the surface. In reality, the effects are three dimensional. From the conservation of mass in three dimensions, a change in velocity in the stream-wise direction causes a change in velocity in the other directions as well. There is a small component of velocity perpendicular to the surface which displaces or moves the flow above it. One can define the thickness of the boundary layer to be the amount of this displacement. The displacement thickness depends on the Reynolds number which is the ratio of inertial (resistant to change or motion) forces to viscous (heavy and gluey) forces and is given by the equation : Reynolds number (Re) equals velocity (V) times density (ρ) times a characteristic length (l) divided by the viscosity coefficient (μ).

$$Re = \text{Inertria Forces} / \text{Viscous Forces} = \rho Vl / \mu$$

Laminar (layered), or turbulent (disordered), the nature of boundary layers depend on the value of the Reynolds number. For lower Reynolds numbers, the boundary layer is laminar and the streamwise velocity changes uniformly as one moves away from the wall, as shown on the left side of the figure. For higher Reynolds numbers, the boundary layer is turbulent and the streamwise velocity is characterized by unsteady (changing with time) swirling flows inside the boundary layer. The external flow reacts to the edge of the boundary layer just as it would to the physical surface of an object. So the boundary layer gives any object an "effective" shape which is usually slightly different from the physical shape. To make things more confusing, the

15

boundary layer may lift off or "separate" from the body and create an effective shape much different from the physical shape. This happens because the flow in the boundary has very low energy (relative to the free stream) and is more easily driven by changes in pressure. Flow separation is the reason for wing stall at high angle of attack. The effects of the boundary layer on lift are contained in the lift coefficient and the effects on drag are contained in the drag coefficient.

2.3. Boundary Layer Parameters:

Three main parameters (described below) that are used to characterize the size and shape of a boundary layer are the boundary layer thickness, the displacement thickness, and the momentum thickness. Ratios of these thicknesses describe the shape of the boundary layer. There are other such thicknesses, but they are not as common.

Boundary Layer Thickness
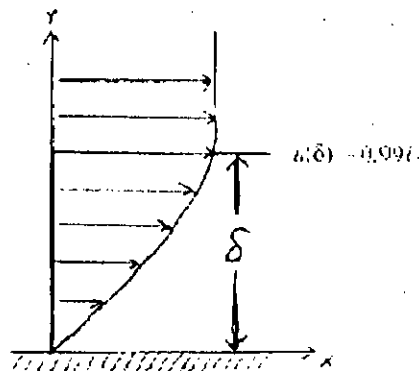
Figure 2.4: Boundary Layer Thickness

The *boundary layer thickness*, signified by δ, shown in figure-2.4, is simply the thickness of the viscous boundary layer region. Because the main effect of viscosity is to slow the fluid near a wall, the edge of the viscous region is found at the point where the fluid velocity is essentially equal to the free-stream velocity.

In a boundary layer, the fluid asymptotically approaches the free-stream velocity as one moves away from the wall, so it never actually equals the free-stream velocity. Conventionally (and arbitrarily), we define the edge of the boundary layer to be the point at which the fluid velocity equals 99% of the free-stream velocity:

$$u|_{y=\delta} \equiv 0.99U$$

Because the boundary layer thickness is defined in terms of the velocity distribution, it is sometimes called the velocity thickness or the velocity boundary layer thickness. Figure 2.4 illustrates the boundary layer thickness.

There are no general equations for boundary layer thickness. Specific equations exist for certain types of boundary layer. For a Blasius (flat-plate, incompressible, laminar) boundary layer, the boundary layer thickness is given by

$$\delta/x = 4.96/\sqrt{(Re_x)}$$

where x is the distance from the leading edge of the plate (Emanuel, 230).

Displacement Thickness

The *displacement thickness*, symbolized by δ^*, shown in Figure- 2.5, is the distance a streamline just outside the boundary layer is displaced away from the wall compared to the inviscid solution. Another way to describe it is the distance the wall would have to be displaced to yield the same solution for flow outside the boundary layer as the boundary layer equations yield.

17
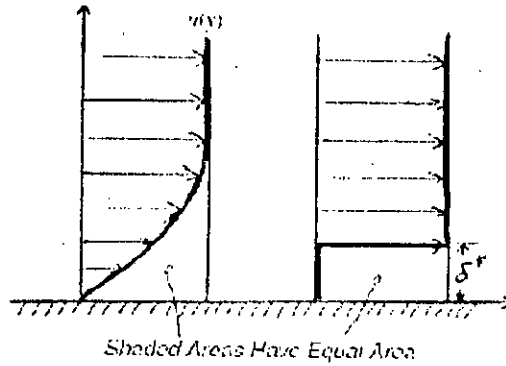
Figure 2.5: Displacement Thickness

Still another way to describe displacement thickness is in figure 2.5. The displacement thickness is the distance that, when multiplied by the free-stream velocity, equals the integral of velocity defect, *(U - u)*, across the boundary layer. That is,

$$U\delta^* = \int_0^\infty (U - u)\,dy$$

Solving for δ^*,

$$\delta^* \equiv \int_0^\infty \left(1 - \frac{u}{U}\right) dy \tag{1}$$

The displacement thickness is important in iterative boundary layer solutions. After employing the boundary layer equations to calculate the displacement thickness along the wall, a virtual wall is created by displacing the wall outward by the displacement thickness. A new inviscid solution is computed using this virtual wall. This yields slightly different free-stream conditions than the initial calculation. The boundary layer solution is then recalculated, using the new free-stream conditions, for the real wall. The process is repeated until the displacement thickness stops moving with each iteration.

18

Momentum Thickness

The *momentum thickness*, symbolized by θ, is the distance that, when multiplied by the square of the free-stream velocity, equals the integral of the momentum defect, *pu(U - u)*, across the boundary layer. That is,

$$\rho U^2 \theta = \int_0^\infty \rho u (U - u)\, dy$$

Solving for θ,

$$\theta \equiv \int_0^\infty \frac{u}{U} \left(1 - \frac{u}{U} \right) dy \qquad (2)$$

The momentum thickness is somewhat harder to visualize than the displacement thickness. One can visualize it using Figure 2.5, except that specific momentum flux distribution $u(y)^2$ replaces the velocity distribution $u(y)$.

The momentum thickness is useful in determining the skin friction drag on a surface. The total skin friction drag per unit depth on the surface is given simply by $\rho u^2 \theta$, evaluated at the trailing edge.

19

2.4. Boundary Layer Equations

The boundary layer equations represent a significant simplification over the full Navier-Stokes equations in a boundary layer region. The simplification is done by an order-of-magnitude analysis; that is, determining which terms in the equations are very small relative to the other terms.

For simplicity, we will determine the boundary layer equations for steady, incompressible (M << 1), uniform flow over a flat plate. The equations for flow over curved surfaces, and for nonuniform flow, differ only slightly, in that they need to account for changes in U along the wall surface. Curved surfaces also require a transformation to surface coordinates. The equations for compressible boundary layers are somewhat more complex than the incompressible equations; we will not consider them here.

Assumptions

The boundary layer equations require several assumptions about the flow in the boundary layer.

1. All of the viscous effects of the flowfield are confined to the boundary layer, adjacent to the wall. Outside of the boundary layer, viscous effects are not important, so that flow can be determined by inviscid solutions such as potential flow or Euler equations.

2. The viscous layer is thin compared to the length of the wall. If L is a characteristic length of the the wall, then $\delta/L << 1$. Also, $x = O(L)$ and $y = O(\delta)$. This assumption is obviously not valid near the leading edge of the wall; other methods (such as stagnation flow) are used to determine the upstream boundary condition.

3. The boundary conditions of the boundary layer region are the no-slip condition at the wall, and the free-stream condition at infinity:

$$u(x, 0) = 0 \qquad v(x, 0) = 0$$
$$u(x, \infty) = U \qquad v(x, \infty) = 0$$

4. In the boundary layer, $u = O(U)$.

Order-of-Magnitude Analysis

For this problem, we consider a two-dimensional, semi-infinite flat plate with its leading edge at the origin. The plate coincides with the positive x-axis. The inviscid flow field is steady, uniform, parallel to the flat plate, with a velocity of U_∞, a density of ρ_∞, and a dynamic viscosity of μ_∞.

The continuity and momentum conservation equations for incompressible, two-dimensional flow are:

$$\frac{\partial u}{\partial x} + \frac{\partial v}{\partial y} = 0 \tag{3}$$

$$\rho\left(u\frac{\partial u}{\partial x} + v\frac{\partial u}{\partial y}\right) = -\frac{\partial p}{\partial x} + \mu\left(\frac{\partial^2 u}{\partial x^2} + \frac{\partial^2 u}{\partial y^2}\right) \tag{4}$$

$$\rho\left(u\frac{\partial v}{\partial x} + v\frac{\partial v}{\partial y}\right) = -\frac{\partial p}{\partial y} + \mu\left(\frac{\partial^2 v}{\partial x^2} + \frac{\partial^2 v}{\partial y^2}\right) \tag{5}$$

To make the order-of-magnitude analysis more straightforward, we shall nondimensionalize the equations. Define nondimensional variables, denoted by an asterisk (u^*, v^*, etc.), by the following:

$$u^* = \frac{u}{U_\infty} \qquad v^* = \frac{v}{U_\infty} \qquad x^* = \frac{x}{L} \qquad y^* = \frac{y}{L}$$

$$\rho^* = \frac{\rho}{\rho_\infty} \qquad p^* = \frac{p}{\rho_\infty U_\infty^2} \qquad \mu^* = \frac{\mu}{\mu_\infty} \qquad Re = \frac{\rho_\infty U_\infty L}{\mu_\infty}$$

21

These definitions, substituted into Equations 3-4, yield the nondimensional continuity and momentum equations:

$$\frac{\partial u^*}{\partial x^*} + \frac{\partial v^*}{\partial y^*} = 0 \tag{6}$$

$$u^* \frac{\partial u^*}{\partial x^*} + v^* \frac{\partial u^*}{\partial y^*} = -\frac{\partial p^*}{\partial x^*} + \frac{1}{Re} \left(\frac{\partial^2 u^*}{\partial x^{*2}} + \frac{\partial^2 u^*}{\partial y^{*2}} \right) \tag{7}$$

$$u^* \frac{\partial v^*}{\partial x^*} + v^* \frac{\partial v^*}{\partial y^*} = -\frac{\partial p^*}{\partial y^*} + \frac{1}{Re} \left(\frac{\partial^2 v^*}{\partial x^{*2}} + \frac{\partial^2 v^*}{\partial y^{*2}} \right) \tag{8}$$

In addition, we define a nondimensional boundary layer thickness $\delta^* = \delta/L$ (not to be confused with the displacement thickness; as this analysis does not use the displacement thickness). By Assumption 2 above, $\delta^* << 1$.

Based on Assumption 4, $u = O(U) = O(1)$. And based on Assumption 2, $x^* = O(x/L) = O(1)$ and $y^* = O(y/L) = O(\delta^*)$. From the continuity equation, Equation 6,

$$\frac{O(1)}{O(1)} + \frac{v^*}{O(\delta^*)} = 0$$

which means that $v^* = O(\delta^*)$. This in turn means that the y-component of velocity is small in the boundary layer.

From the x-momentum equation, Equation 8,

$$O(1)\frac{O(1)}{O(1)} + O(\delta^*)\frac{O(1)}{O(\delta^*)} = -\frac{\partial p^*}{\partial x^*} + \frac{1}{Re} \left(\frac{O(1)}{O(1)} + \frac{O(1)}{O(\delta^{*2})} \right)$$

It should be noted that we have made no assumptions about pressure, and so we do yet not know its order of magnitude. For now, we keep the pressure gradient term.

22

Considering the two viscous terms, we see that the first viscous term, which is of order $1/Re$, is very small compared to the second term, which is of order $1/(Re\delta^{*2})$. We therefore drop the first term, which corresponds to the term $\partial u^*/\partial x^*$ in Equation 7.

According to Assumption 1, the region near the wall is a viscous boundary layer. In order to keep the remaining viscous term important (but not have it dominate), the term must be of order one, to match the order of the convective terms. Thus, Re must be of order $1/\delta^{*2}$.

We see, then, that the assumption of a thin boundary layer is reasonable only for flows where $Re \gg 1$. Fortunately, this is true of many flows. However, for flows of very viscous or very slow fluids, the thin boundary layer is not a reasonable assumption.

Now, we expect any changes in pressure along the boundary layer to affect the boundary layer. Therefore, we assign pressure an order of magnitude of 1 so that $\partial p^*/\partial x^* = O(1)$ to match the other terms. (There will not be any pressure changes for the flat plate, but we keep this term in the interests of generality.)

Now, from the y-momentum equation, Equation 8,

$$O(1)\frac{O(\delta^*)}{O(1)} + O(\delta^*)\frac{O(\delta^*)}{O(\delta^*)} = -\frac{O(1)}{O(\delta^*)} + \delta^{*2}\left(\frac{O(\delta^*)}{O(1)} + \frac{O(\delta^*)}{O(\delta^{*2})}\right)$$

The pressure gradient term is of order $1/\delta^*$. Every other term in this equation is at most of order δ^*. All of the other terms are very small compared the to the pressure gradient term, and to the terms from the continuity and x-momentum equations. Hence, the pressure gradient term is the only term that is retained from Equation 8.

Equation 8 reduces to $\partial p^*/\partial y^* = 0$. This says that the pressure difference across the boundary layer is essentially zero. This is why inviscid solutions have reasonable success: they can predict the pressure distribution on a surface with considerable accuracy because the boundary layer does not affect the pressure that much.

So, after the order of magnitude analysis, Equations 6-8 become:

$$\frac{\partial u^*}{\partial x^*} + \frac{\partial v^*}{\partial y^*} = 0 \tag{9}$$

$$u^*\frac{\partial u^*}{\partial x^*} + v^*\frac{\partial u^*}{\partial y^*} = -\frac{\partial p^*}{\partial x^*} + \frac{1}{Re}\frac{\partial^2 u^*}{\partial y^{*2}} \tag{10}$$

$$0 = \frac{\partial p^*}{\partial y^*} \tag{11}$$

The continuity equation does not simplify at all. The x-momentum equation, however, loses a second order term. In the process, it changes from elliptic to parabolic in nature. Because parabolic equations are easier to solve numerically than elliptic equations, this is very significant simplification. Also, the y-momentum equation basically disappears, which is a tremendous simplification.

The boundary layer equations can be used in dimensional form as well:

$$\frac{\partial u}{\partial x} + \frac{\partial u}{\partial y} = 0$$

$$\rho\left(u\frac{\partial u}{\partial x} + v\frac{\partial u}{\partial y}\right) = -\frac{\partial p}{\partial x} + \mu\frac{\partial^2 u}{\partial y^2}$$

$$0 = \frac{\partial p}{\partial y}$$

Although these equations have been obtained by considering uniform flow over at a flat plate, they are valid for curved surfaces also, as long as the curvature of the surface is not too great. Instead of using Cartesian coordinates x and y, the surface coordinates s and n are used on curved surfaces. Also, the pressure gradient term, $\partial p/\partial x$, is not zero for curved surfaces.

24

2.5 Flow Separation

When the air is unable to follow an object's shape it separates. This is shown in the figure 2.6 for an aerofoil, which while being a streamlined shape, will cause flow separation if it is tilted so that it is more oblique to the flow. This is known as aerofoil *stall*. In order to prevent flow separation it is best to avoid sharp profile changes in flow direction, but making a smooth shape with slow changes in curvature sometimes not possible due to physical limitations. Hence, the design of what we typically call streamlined body shape is actually an attempt at eliminating flow separation. This is usually possible, such as with an aerofoil with a sharp trailing edge, but practical consideration do not always allow us the freedom to build the perfect shape.
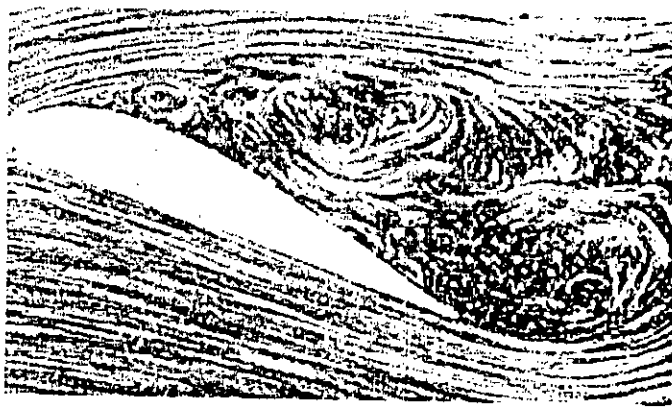
Figure 2.6: Flow separation on an aerofoil shape which is at high angle of attack
(**Source: http://www.nationmaster.com/encyclopedia/Flow-separation**)

There is another way to prevent flow separation though. This relates to boundary layers. Turbulent boundary layers may cause more skin friction drag, but they tend to be thicker and separate later. So for objects in which the pressure drag is dominant, it can be beneficial to artificially trigger a boundary layer to go turbulent to reduce the flow separation effect. This phenomenon is shown in figure 2.7 Laminar boundary layer on smooth ball separate at half way causing a wide wake near pressure drag while the roughness created by and dimples on the surface of a golf ball delays separation past half way around the ball reducing significant pressure drag.

25
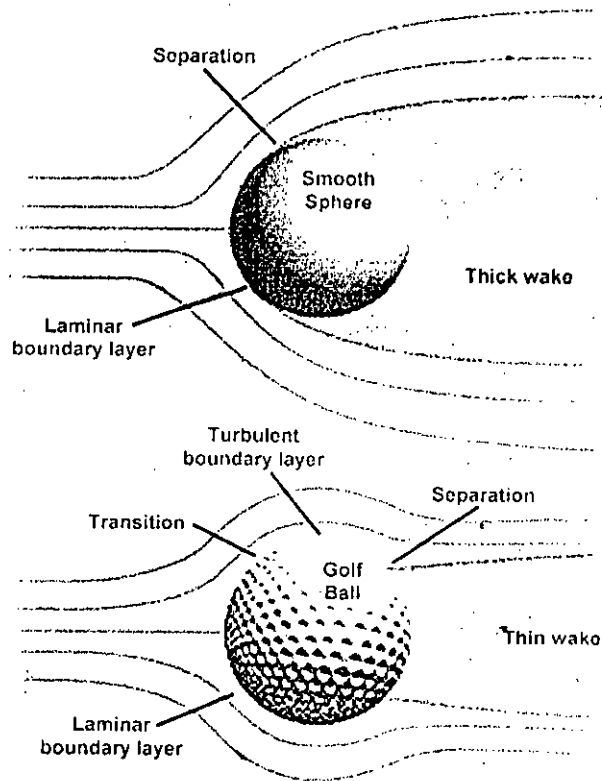
Figure 2.7: Laminar and Turbulent boundary layer on smooth and rough surface
(Source: Aerospace web.org)

The study of flow separation from the surface of a solid body, and the determination of global changes in the flow field that develop as a result of the separation, are among the most fundamental and difficult problems of fluid dynamics. It is well known that most liquid and gas flows observed in nature and encountered in engineering applications involve separation. This is because many of the "common" gases and liquids, such as air and water, have extremely small viscosity and, therefore, most practical flows are characterized by very large values of the Reynolds number; both theory and experiment show that increasing Reynolds number almost invariably results in separation. In fact, to achieve an unseparated form of the flow past a rigid body, rather severe restrictions must be imposed on the shape of the body.

In the case of a favorable pressure gradient, since the pressure gradient tends to accelerate the fluid in the boundary layer, the pressure gradient counteracts partly the retarding action of the viscous stresses. In the case of an unfavorable pressure gradient, however, the problem is more

26

complicated. The fluid near the wall now must not only overcome the wall shear stress, but it must also flow against the unfavorable pressure gradient. In contrast to this, the fluid near the outer edge of the boundary layer needs only to flow against the un-favorable pressure gradient, since the shear stress there is much smaller. As a consequence, the fluid near the wall is decelerated more rapidly. It may eventually be forced to flow backward. At the point where this flow reversal first occurs, the slope of the velocity profile, $\partial U/\partial y$, at the wall must be zero. This point is called the separation point, and is illustrated in figure: 2.8.

Velocity profiles
(Boundary layer thickness exaggerated)

Streamline pattern
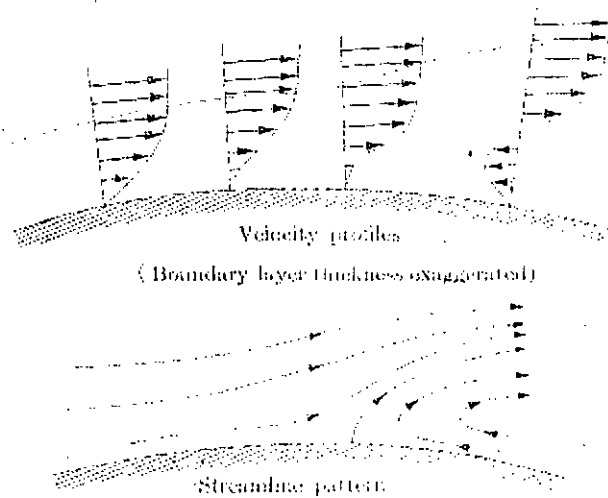
Fig- 2.8: Illustration of flow separation though velocity profiles

The difference between a separated flow and its theoretical unseparated counterpart (constructed solely on the basis of inviscid flow analysis) concerns not only the form of trajectories of fluid particles, but also the magnitudes of aerodynamic forces acting on the body. For example, for bluff bodies in an incompressible flow, it is known from experimental observations that the drag force is never zero; furthermore, it does not approach zero as the Reynolds number becomes large. On the other hand, one of the most famous results of the inviscid flow theory is d'Alembert's paradox which states that a rigid body does not experience any drag in incompressible flow. It is well known that this contradiction is associated with the assumption of a fully attached form of the flow; this situation almost never happens in practice.

27

Separation imposes a considerable limitation on the operating characteristics of aircraft wings, helicopter blades, turbines, etc., leading to a significant degradation of their performance. It is well known that the separation is normally accompanied by a loss of the lift force, sharp increase of the drag, increase of the heat transfer at the reattachment region, pulsations of pressure, as a result, flutter, and buffet onset.

Separation and reattachment processes involve generation and interaction of shear layers. It is known that turbulent shear flows are very sensitive to small changes in initial or boundary conditions and to different types of upwind, downwind and separation point perturbations applied during transition (Cantwell, 1981; Oster and Wygnanski, 1982). Thus, a particular airfoil sensibility to specific characteristics of flow and environmental perturbations is quite probable. Exploring this perception Green and Galbraith (1994) demonstrated aspects of the effect of the testing environment on unsteady aerodynamical experiments. Numerous experimental studies have also shown the significant effects of particular external perturbations on airfoil performance. If these perturbations are able to induce flow variations at an appropriate frequency, then significant boundary layer separation phenomena may be controlled allowing improvements in airfoil performance (Mueller and Batill, 1982; Zaman 1992). The unsteady mechanisms that might produce these effects are still obscure. By way of illustration, the discrepancies of experimental and numerical results shown by McGhee *et al.* (1988), confirm the complexity of these phenomena. More recently Swalwell *et al.* (2003) investigated experimentally effects of turbulence intensity generated by different grids on the stall of a thick NACA 4421 airfoil section with an aspect ratio greater than seven, for angles of attack ranging from -90° to +90°, at a Reynolds number of 2.85×10^5. The realism of this turbulence generation is questionable because grid generated turbulence is quite different from the turbulence within the atmospheric surface layer. Conventional aerodynamic theory is still not capable of predicting the real forces generated by wings submitted to brusque variations of angle of attack. It has been recognized for many years that the maximum lifting force generated by a wing compelled to rapid pitching motion can be substantially enhanced. These conditions may occur in rapidly maneuvering aircraft, flapping wings, wind turbines in gusty wind, flight operations in turbulent environment or flying through the wake of other airplanes. It has been learned that when an airfoil is submitted to rapidly increasing angles of attack above the stationary separation point a

28

strong vortex, located on the suction surface is usually generated. This vortex is called dynamic stall vortex. After growing to a given size, this eddy may be shed downstream into the wake flow. Typically, the lift increases with increasing vortex intensity. As long as the vortex remains close to the upper surface of an airfoil a substantial lift increase occurs, which decreases rapidly as the vortex flows away. The basics of this dynamic stall process have been described by McCroskey (1982), Carr *et al.*, (1977) and Carr (1985). The limitations of the existing methodologies for predicting, calculating and describing the time dependent location and nature of separated regions induce the unavoidably requirement of experimental work. Many Researchers performed experiments in order to contribute to the understanding of turbulent scale dependent effects on the behavior of low Reynolds number airfoils and to present data against which airfoil prediction methodologies can be tested.

2.6 Boundary Layer Control

Boundary-layer control is a wise and efficient method of increasing the lift coefficient C_L. The idea is

1. Either to remove the low-energy segment of the boundary layer and let it be replaced by high-energy flow from above

2. or by adding kinetic energy to the boundary layer directly. Both of these methods maintain a laminar flow for a longer distance over the airfoil, delay separation, and allow one to get a larger angle of attack before stall occurs, and thus a higher C_L.

The slot was shown to be one means of passing high-energy flow over the top surface of a wing.

The low-energy boundary layer may be sucked through slots or holes in the wing as shown in figure-2.8(a) or high-energy air may be blown into the boundary layer through backward facing holes or slots as shown in figure 2.8(b).

(a) Suction of boundary layer.

(b) Reenergizing the boundary layer.
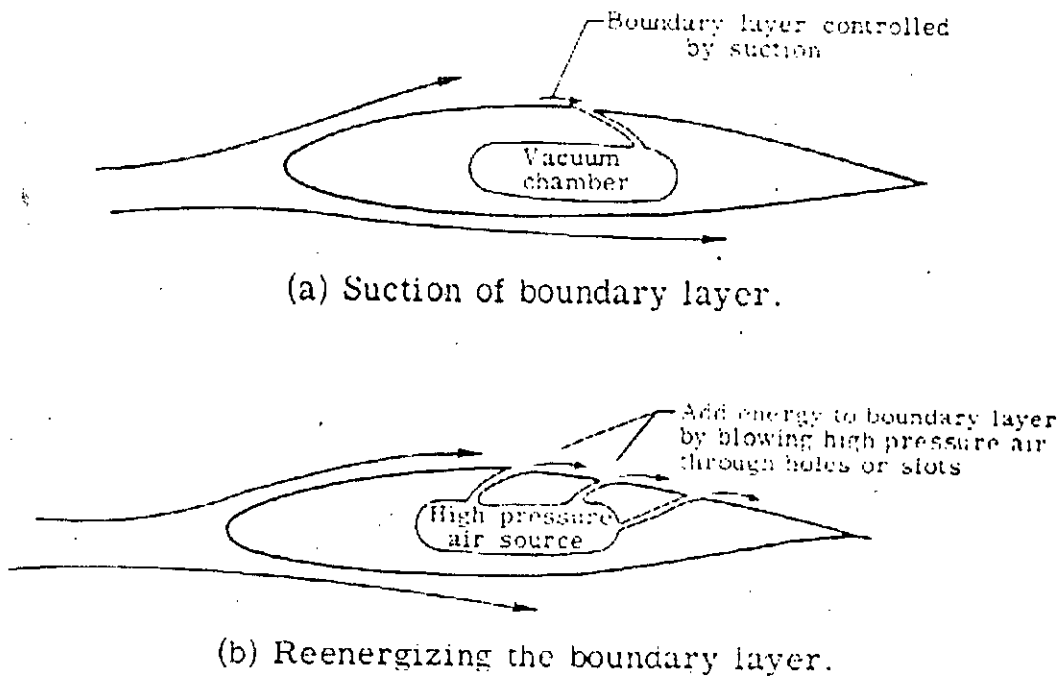
Figure- 2.8: Boundary layer control (a) suction and (b) high pressure discharge

Again, boundary layer control is also done by slats, shown in figure- 2.9, which create slot that act as a venture tube and thus energize the boundary layer.
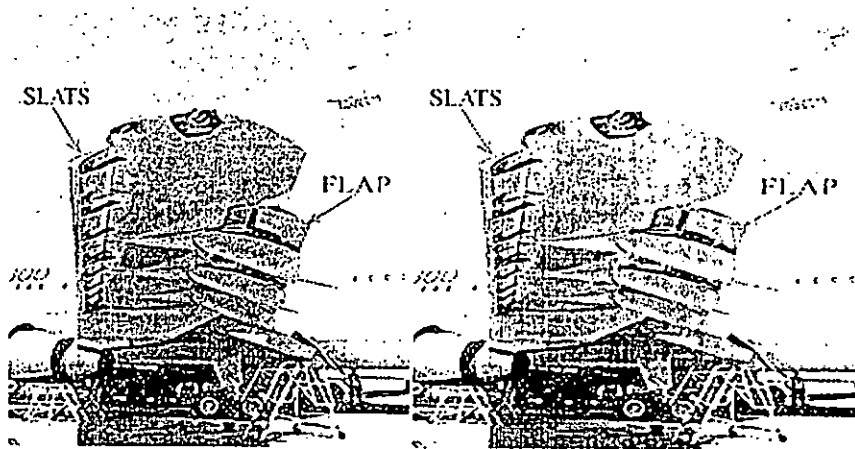
Figure- 2.9: Slats employed to control the boundary layer

Vortex generators are also used for the purpose of boundary layer control. They are aerodynamic surfaces, consisting of small vanes that create a vortex. However, this vortex creation does not add a negative impact on aircraft aerodynamics; rather they just reenergize the sluggish boundary layer. Vortex generators can be found on many devices, but the term is most often used in aircraft design. Figure- 2.10 shows vortex generator vanes on an aircraft wing.

Figure 2.10: Vortex generator vanes on the wing of an aircraft

31

2.7 Airfoil Geometry and Coordinate System

Airfoil geometry can be characterized by the coordinates of the upper and lower surface. It is often summarized by a few parameters such as: maximum thickness, maximum camber, position of max thickness, position of max camber, and nose radius. One can generate a reasonable airfoil section given these parameters. This was done by Eastman Jacobs in the early 1930's to create a family of airfoils known as the NACA Sections. To describe the geometry of airfoil sections, the following terms are used:
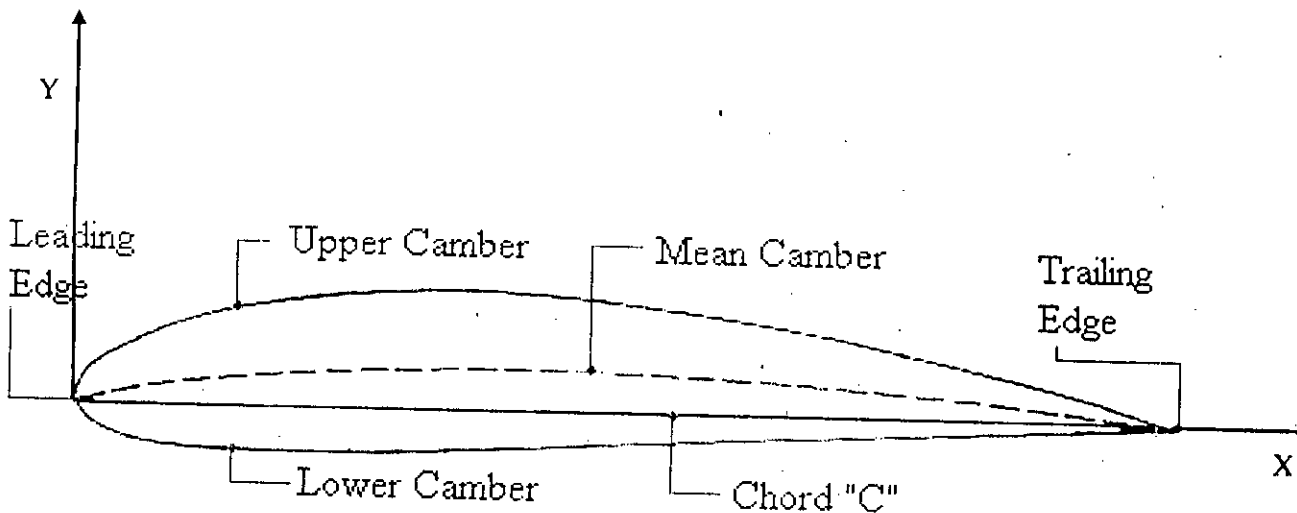
Figure 2.11: Airfoil section showing different geometrical terms.

- Mean line or mean chamber line is the line representing the locus of all points midway between the upper and lower surface of an aerofoil as measured perpendicular to the mean line.
- Chord line is the line joining the ends of the mean camber line.
- Thickness is the height of the profile measured perpendicular to the cord line.
- Camber or the maximum camber is the maximum rise of the mean line from the cord line.
- Leading edge radius is the radius of a circle, tangent to the upper and lower surfaces, with its centre located on a tangent to the mean-camber line drawn through the leading edge of this line. The leading edge radius is also given in percent of the chord.

These definitions are illustrated in Figure 2.11.

Chapter 3

ABOUT THE MODEL

A fuselage with NACA 2412 aerofoil cross-section is made of wood teak with satisfactory surface finish. To reduce interference drag at the interface of wing and fuselage the fuselage is given an aerodynamic shape.

For pressure measurements three-tube yaw meter probe is used. The pressure connections are made through small diameter tygon tubes and are connected to the digital pressure transducer through the selector valve.

Wings:

As four digit sections are suitable for low speed aircraft so for both wings and aerofoiled fuselage NACA four digit series aerofoil are considered in the present investigation. Same set of wings are used in both the type of models so that the results would show the comparison between the fuselages.

NACA Four-Digit Series:

The first family of airfoils designed using this approach became known as the NACA Four-Digit Series. The first digit specifies the maximum camber (m) in percentage of the chord (airfoil length), the second indicates the position of the maximum camber (p) in tenths of chord, and the last two numbers provide the maximum thickness (t) of the airfoil in percentage of chord. For example, the NACA 2412 thickness of 12% with a camber of 2% located 40% back from the airfoil leading edge (or 0.4c).

The **NACA 2412** cambered aerofoil wings with a chord length of 80 mm and a total span of 200 mm is used for the model, which has an aerofoiled fuselage of NACA 2412; 240 mm chord and 100 mm span. Figure 3.1 shows the cross-section of an **NACA 2412** cambered aerofoil wing section.
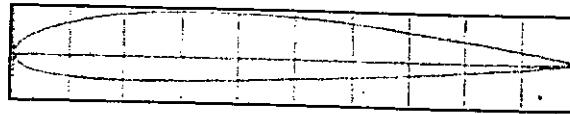
Figure 3.1: The real size cross-section of the model wings

The wings and all the fuselages are manufactured from a single piece of teak wood which has a density of approximately 650 kg/m^3
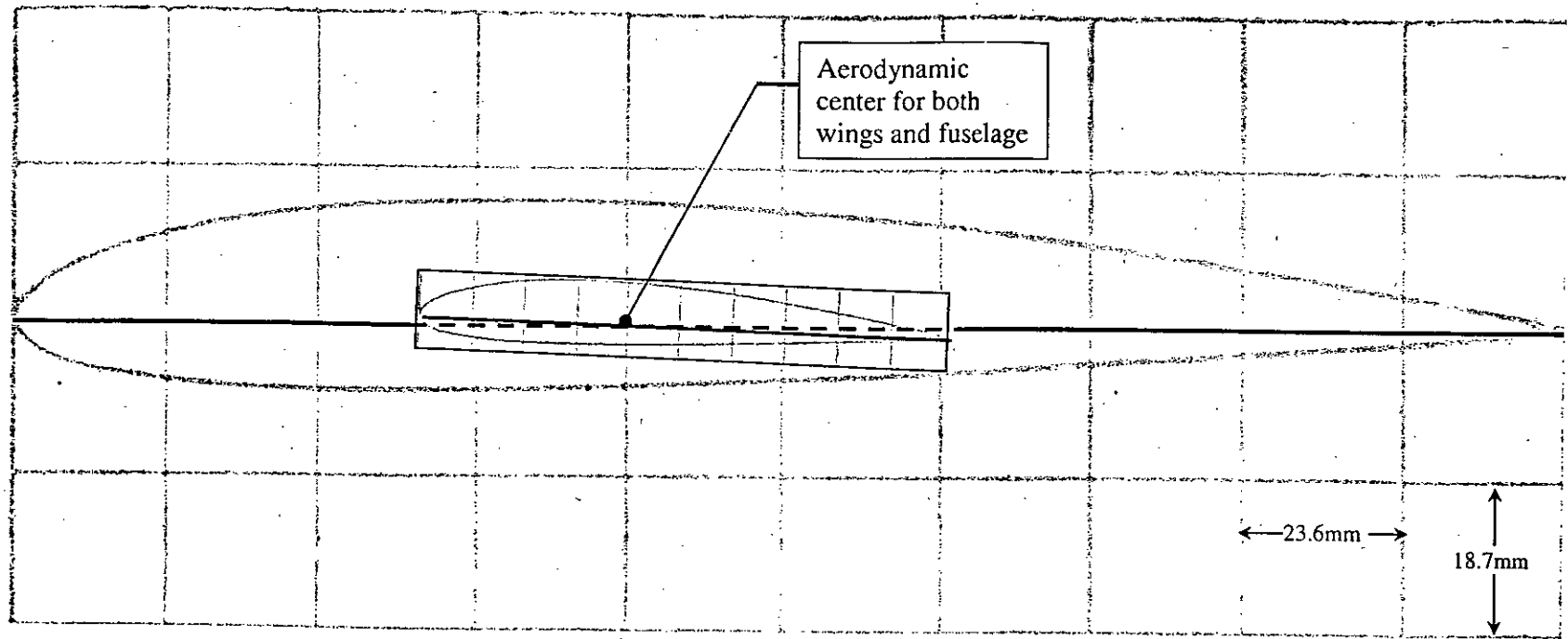
Figure 3.2: The real size cross section of the model aerofoiled fuselage, showing the wing position
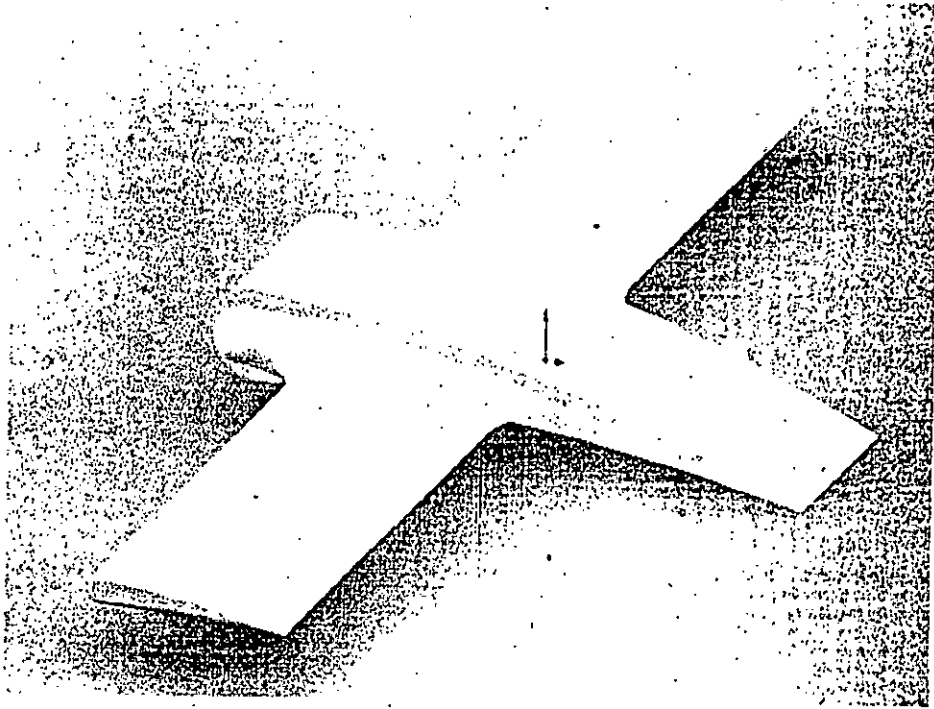
Figure 3.3: 3D view of the model plane with aerofoil fuselage
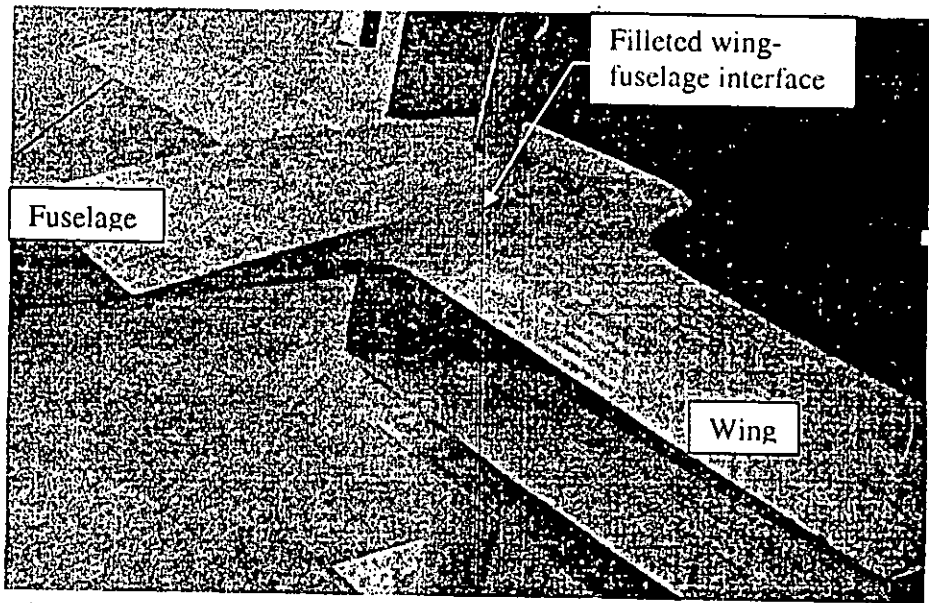
Figure 3.4: Photograph of the model plane with aerodynamic-shaped aerofoil fuselage and filleted wing-fuselage interface to reduce interference drag

36

Chapter 4

EXPERIMENTAL SETUP

The experiment is done in a 700mm×700mm size closed circuit wind tunnel with the models to find the velocity profiles over the wing and fuselage and to find the flow direction. The tunnel section, the yaw meter probes, the pressure transducer, the pressure probe selection box together with the traversing mechanism are the main part of the test setup.

4.1. Wind tunnel:

The experiment is carried out in a 700mm×700mm closed circuit wind tunnel as shown in Figure 4.1. The wind tunnel is powered by the two 700mmD counter rotating Woods (U.K.) aerofoil fans. To minimize transmission of vibration generated in the fans unit, it is mounted in a separated heavy foundation and is connected to the rest of the wind tunnel by two vibration isolators made of heavy canvas cloth at both side of the fan unit. At the discharge of the fans there is a silencer to reduce the sound level. From the silencer air flow passes through the flow controlling butterfly valve, diffuser and the plenum chamber to stabilize the flow to certain level. Air from the plenum chamber passes over the cooling coil and through the air filter before entering the parabolic contraction cone. In the contraction cone the dimension is reduced from 1525mm×1525mm to 700mm×700mm. at the delivery of the contraction cone where there is a honey comb flow strainer to straighten out any flow diversity and break down any large eddy before entering into the 9m long test section. Flow form the test section goes back to the fan unit through the return duct. The fan motors are powered by 400V-3Φ-50Hz power supply through motor speed controller. Thus the wind speed in the tunnel can be varied both by controlling the fan motor speed as well as by controlling the butterfly valve. For better understanding of the Wind Tunnel details of some of its major components are illustrated below:

- **Fan Unit:** The fan unit consists of two counter rotating axial flow fans powered by centrally mounted 22 kW a.c. motors. The blades of the fans are adjustable to minimize the power loss and sound generated in the fan blades; its angles are set such that the flow enters in both the fan blades tangentially without any shock. By changing the blade angles of both the fans flow velocity range in the wind tunnel can be changed.

- **Air Speed:** In the present setup of fan blade angle setting the maximum air speed is 44.5 m/s (160km/hr) which can be increase to as high as 70m/s (250 km/hr) by changing the blade angles of the fans. The air speed can be varied by two different ways; i) by using an electronically controlled butterfly valve and ii) by controlling the motor speed by an electrical frequency converter. The later one is more convenient to change the air speed smoothly and frequently from zero to any required velocities. In this experiment the frequency converter is used to vary the air speed.

- **Air Temperature Controlling:** In a close circuit wind tunnel as the same air circulates inside the tunnel so the air temperature increases due to adiabatic power transfer from the rotating blades to the flowing air and the friction loss in the tunnel. A 16 ton DX cooling coil is used to control the air temperature to the required level. However it does not require to control the air temperature as in the present investigation test is carried out in the open section and the velocities of air are comparatively low. Although at low speed it produces some heat if the tunnel runs continuously for a long time, so to avoid this, the tunnel was allowed to shutdown for a while after taking each set of data.

4.2. Test sections:

The tunnel has seven 700mm×700mm test sections. To facilitate the present experiment to be carried out in the open air condition the diffuser connected at the end of the last test section is taken out and to avoid the buffer effect of the discharge side of the test section is fitted with a 700mm×700mm discharge duct and to provide a shock less entry a 1000mm×1000mm to 762mm×762mm bell mouth entry is added at the return duct. Thus a 700mm×700mm×406mm open flow field created between the discharge duct and the bell mouth entry become the experimental space where desire velocity is obtained. Figure 4.1 shows the detail out line of the Wind Tunnel.

Figure 4.1: 700mm × 700mm closed circuit Wind Tunnel

Figure 4.2: Actual photograph of the 700mm × 700mm closed circuit Wind Tunnel
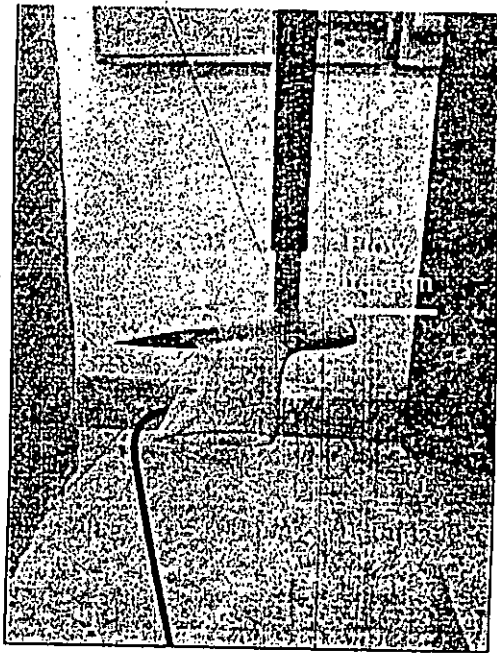
Figure- 4.3: Photograph of the test-section

40
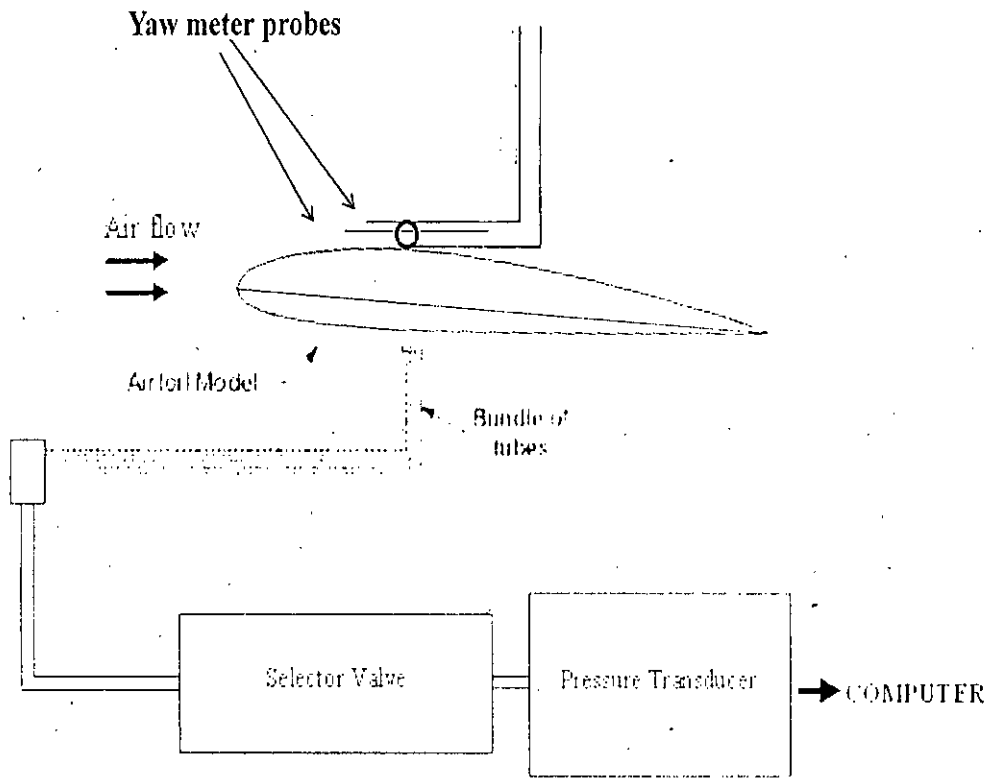
Figure- 4.4: Schematic Diagram of the experimental set-up

As air flows over the model, the three tubes of the yawmeter probe senses corresponding pressures. This pressure is read from the pressure tranducer by selecting the intended tube from the selection box. The data is then recorded in a computer and analysed. Figure- 4.4 shows a schematic view of the experimental set up. A total picture of the experimental set up is presented in figure- 4.5.

Pressure Transducer

Computer

Selection Box

Support Frame

Support bar with aerodynamic shape

The Model

Yawmeter Probe

Traversing Mechanism

Figure 4.5: Photograph of the Experimental Set-up

Chapter 5

EXPERIMENTAL PROCEDURE

5.1. Working Principle

A three-tube yawmeter probe along with a pressure transducer and a selection box is the main the main instrument used in this research. To find the velocity profile at different chord-wise stations on the wing and the fuselage, the yawmeter probe is placed at the desired point with the help of a traversing mechanism.

For pressure measurements the pressure connections were made through small diameter tygon tubes and were connected to the digital pressure transducer through the selector valve. A three-tube yawmeter is used to measure velocity profile and flow direction over the wing and fuselage and all of the three tubes were connected to the selector valve which acted like a multiplexer. So, to set 1 in the selector valve means the digital pressure transducer are all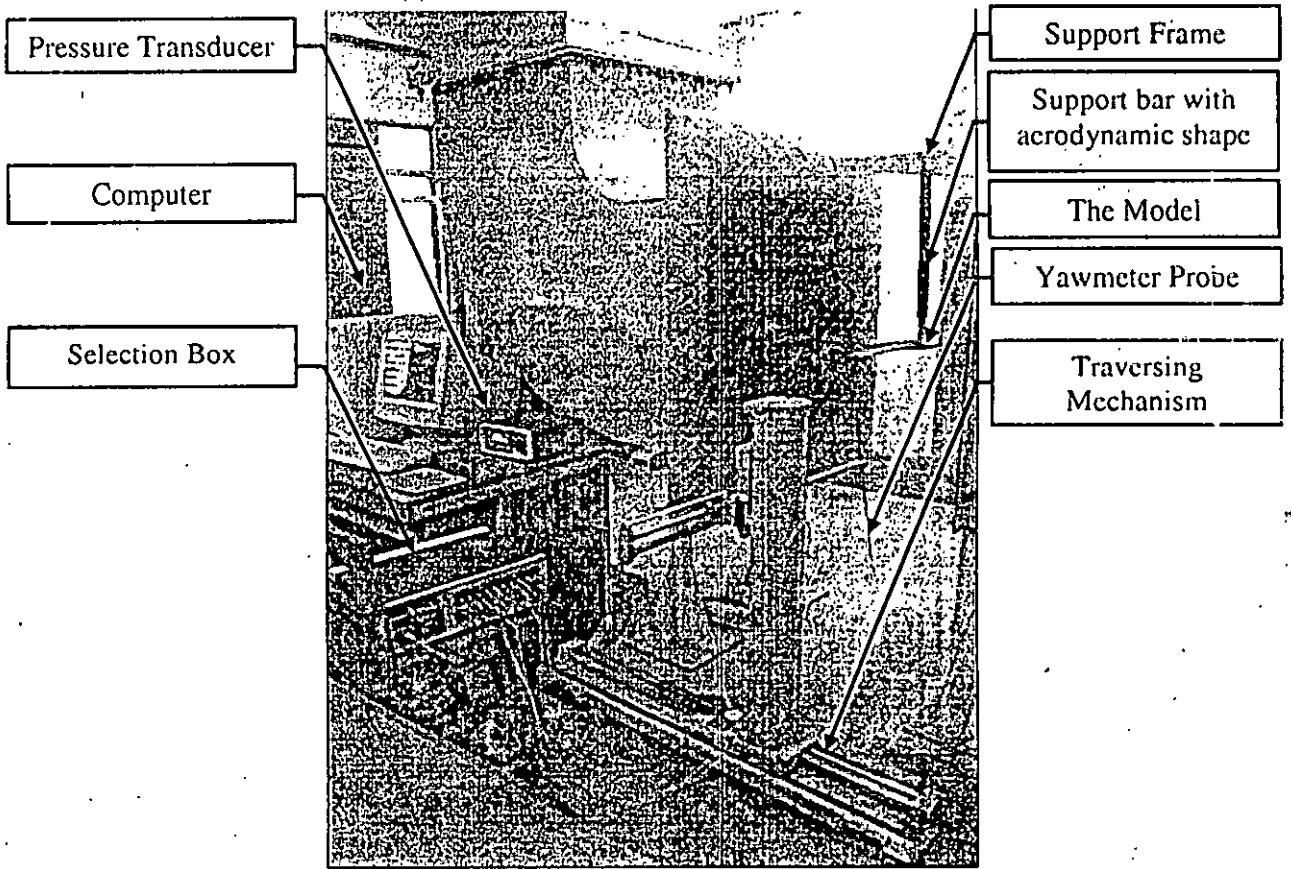owed to show the pressure on the first probe. Before taking any data sufficient time were allowed to make the digital transducer become stable to a certain value. The corresponding pressures were recorded in the computer and then applying proper equations the velocities and flow angle were calculated.

The whole experiments were carried out for two different speeds, viz 30 km/hr and 40 km/hr with an angle of attack of both the fuselages and the wings at 4°, the angle of attack for maximum lift to drag ration as found by previous researcher.

5.2. Flow field examination

Before starting the experiment with the models the flow field of the test section is examined with the help of a transverse mechanism. As the whole experiment was carried out for different air velocities so the flow field was also examined for those velocities. The following table shows the grid velocities at different air speeds.

Table 5.1: Flow field analysis (U/U_a at different grid points in test section)

| Distance from the surface of the tunnel, mm	Air velocity (km/hr)							
	30	40	50	60	70	80	90	100
2	0.61	0.69	0.67	0.65	0.68	0.68	0.69	0.72
10	0.76	0.84	0.82	0.79	0.78	0.81	0.79	0.8
20	0.83	0.87	0.83	0.86	0.84	0.86	0.85	0.85
30	0.86	0.9	0.87	0.9	0.88	0.88	0.88	0.89
40	0.88	0.95	0.9	0.91	0.9	0.9	0.91	0.9
50	0.9	0.96	0.93	0.92	0.94	0.93	0.92	0.93
60	0.92	0.98	0.94	0.95	0.95	0.94	0.93	0.95
70	0.97	0.99	0.94	0.98	0.96	0.95	0.98	0.96
80	1	1	0.98	0.99	0.97	0.97	0.98	0.97
90	1	1	1	1	0.98	0.99	0.99	0.98
100	1	1	1	1	1	1	1	0.99
110	1	1	1	1	1	1	1	1
120	1	1	1	1	1	1	1	1
210	1	1	1	1	1	1	1	1
300	1	1	1	1	1	1	1	1
350	1	1	1	1	1	1	1	1
400	1	1	1	1	1	1	1	1
490	1	1	1	1	1	1	1	1
580	1	1	1	1	1	1	1	1
590	1	1	1	1	1	1	1	1
600	1	1	1	1	1	1	1	0.99
610	1	1	1	1	0.98	0.99	0.99	0.98
620	1	1	0.98	0.99	0.97	0.97	0.98	0.97
630	0.97	0.99	0.94	0.98	0.96	0.95	0.98	0.96
640	0.92	0.98	0.94	0.95	0.95	0.94	0.93	0.95
650	0.9	0.96	0.93	0.92	0.94	0.93	0.92	0.93
660	0.88	0.95	0.9	0.91	0.9	0.9	0.91	0.9
670	0.86	0.9	0.87	0.9	0.88	0.88	0.88	0.89
680	0.83	0.87	0.83	0.86	0.84	0.86	0.85	0.85
690	0.76	0.84	0.82	0.79	0.78	0.81	0.79	0.8
698	0.61	0.69	0.67	0.65	0.68	0.68	0.69	0.72

Uniform flow regime
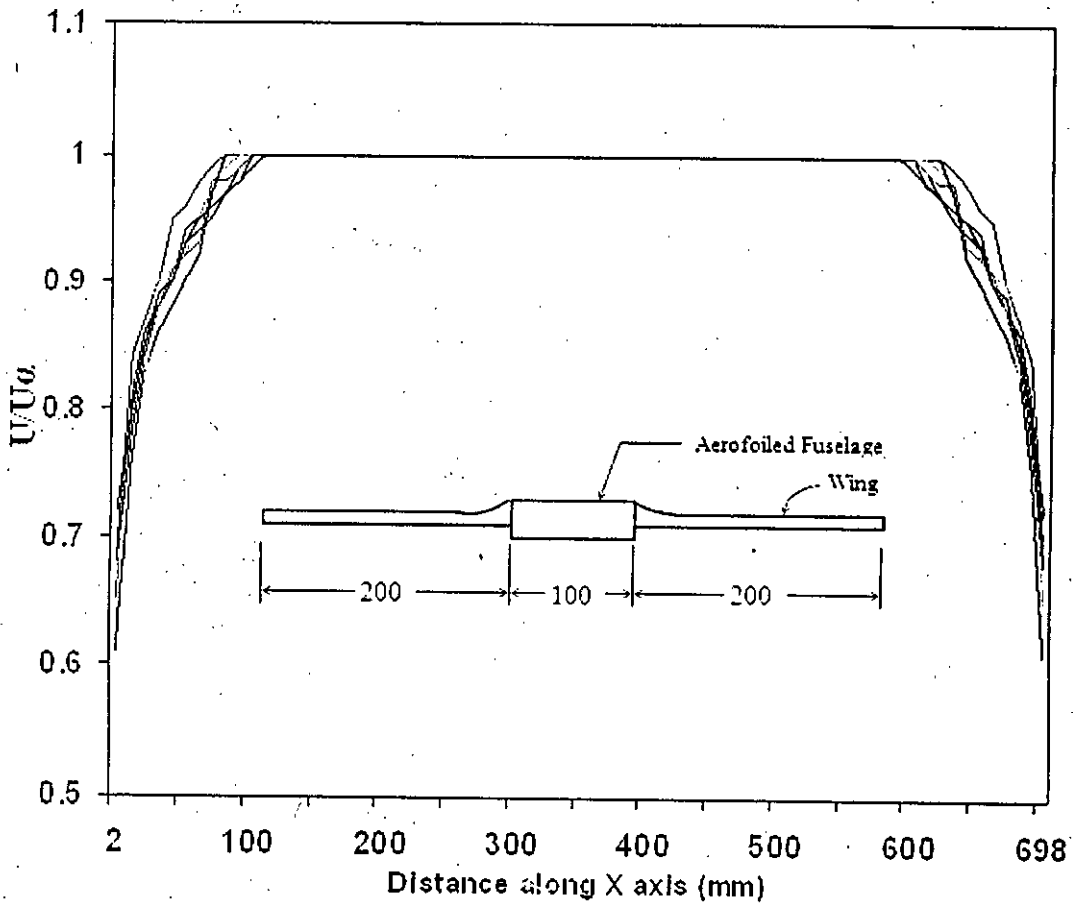
Figure 5.1: Flow field showing the in uniform flow regime

From figure 5.1 it found that the boundary layer increases as flow velocity increase and at maximum air speed the boundary layer consume 100mm at one side i,e 200mm for both side along any axis. Since at test section the tunnel cross section is 700mm×700mm, so considering boundary layer the uniform flow regime become 500mm×500mm. As the maximum width of the models is 500mm and maximum height is 50mm so the model is in uniform flow regime even when the air velocity is maximum, as shown in figure 5.1.

Chapter 6

RESULTS AND DISCUSSION

6.1 Introduction

In this investigation, angle of attacks of both the fuselage (θf) and wing (θw) were fixed at 4°, the angle of attack for highest lift to drag ratio (L/D) as found by the previous researcher. The investigation is carried out for two speeds, viz 30 km/hr and 40 km/hr. The nature of boundary layers over the wings and the aerofoiled fuselage are investigated. Velocity profiles and flow angles are measured with the help of three tube yaw meter, for both upper and lower surfaces of both aerofoils i.e. the wing and the fuselage.

Velocity profiles are measured over the wing at its centre at 30 km/hr speed. Then the whole experiment is repeated at the centre of the fuselage which is the same airfoil like the wing NACA 2412 but with a chord length three times that of the wing. Velocity profiles for both the cases are shown.

After making observations on the change of the shape of the velocity profiles over both of the aerofoils for different positions along chord, a similar investigation is done again at the speed of 40 km/hr. In the second case again, the velocity profiles are drawn over both the aerofoils. Observations are made to understand the change of velocity profile as we move along the chord. To compare the nature of boundary layer over the same aerofoil with different chord length, velocity profiles at nearly same percentage of chord are put together and observations made.

A complete understanding of how lift and drag forces are produced on aerofoils needs the investigation of the flow field over the upper surface of the aerofoil as well as under its lower surface. Hence, the total investigation for both the speeds are repeated under the lower surface of the wing and the fuselage. Like the upper surface, velocity profiles are also drawn for both speeds—30 km/hr and 40 km/hr and finally observations made in a similar manner to that for the upper surface. The curves for each case and their findings are discussed in the following sections.

6.2 Velocity Profiles and Flow Angle over the Wing

At first the nature of the boundary layer and wake formation and separation over the upper surface of the wing is studied. Investigations are done at two wind speeds 30 km/hr and 40 km/hr (subsections 6.2.1 and 6.2.2 respectively). Then the same investigations were done for the lower surface of wing at the two speeds (subsection 6.2.3). For all the experiments, yaw meter probes are set at appropriate position and the corresponding deflections given by the pressure transducer were recorded in a computer, speed determined and flow angle found.

For convenience the following symbols are used in all the data tables:

θf => Fuselage angle of attack in degree

θw => Relative angle between wing and fuselage (= zero for present investigation)

X => horizontal distance from leading edge

y => vertical distance from the surface

δ => boundary layer thickness

U_∞ => free stream velocity in X- direction

U => local velocity in X- direction

In this section velocity profiles on both the upper and lower surfaces of the wing are presented and its characteristics features are analysed for better understanding of the flow field in this region. Profiles for the velocities U_∞= 30 km/hr and U_∞ = 40 km/hr are presented separately.

6.2.1 Velocity profiles on the upper surface of the wing at $U_\infty = 30$ km/hr

For different position along the chord of the wing, velocity profiles are found out by positioning the measuring probe at different vertical distances from the surface. From the readings of the three probes of the yaw meter, the flow angles are also calculated. For different positions along chord, velocity profiles are plotted and presented in figures 6.2.1(i) to 6.2.1(ix).

Due to the curvature of the airfoil surface of both the wing and the fuselage, the measuring probe can not be placed near the surface of their leading edge zone and so measurements are taken form 22.5% of chord length.

In figure 6.2.1(i), velocity profile near the surface is nearly vertical before taking the usual parabolic shape at about $y/C = 0.008$. This behavior of the velocity profile indicates the condition of boundary layer separation, which actually is found in following station in figure 6.2.1(ii) where separation occurs at about $y/C = 0.008$.

From the curves, it is seen that at 30 km/hr speed over the wing, separation begins nearly at 25% of chord from the leading edge (figure 6.2.1(ii)) and continues till 50% of the chord (figure 6.2.1(iv). It is found that the separation intensifies as we move from 25% of the chord to 50%, and finally at 62.5% separation does not exist any more. Therefore, it can be concluded that the zone of separation is approximately between 25% and 55% of chord length. However, the slope of velocity profile at 22.5% of chord length is nearly zero, which is a strong indication that separation point is close to this 22.5% of the chord length. Finally, near the trailing edge, the boundary layer becomes sluggish, which may also be due to the separation.

6.2.2 Velocity profiles on the upper surface of the wing at $U_\infty = 40$ km/hr

The wind tunnel speed is set at 40 km/hr with help of variable frequency drive. For different position along the chord of the wing, here too, velocity profiles are found out by positioning the measuring probe at different vertical distances from the surface. From the readings of the three tubes of yaw meter, the flow angles are also calculated. For different positions along chord, velocities and flow angles at different vertical distances are given in the table Appendix- (A) 6.2.2 (i) to 6.2.2(b) (ix). With the help of the table corresponding graphs are plotted in figures 6.2.2(i) to 6.2.2(ix).

By comparing figures 6.2.1(i) and 6.2.2(i), it is found that the boundary layer thickness is higher at lower speed and rate of generation of separation zone slower but wider.

From the curves, it is found that at this 40 km/hr speed over the wing, separation begins nearly at 25% of chord from the leading edge (figure 6.2.2(ii)) and continues till 37.5% of the chord (Figure 6.2.2 (iii)). It is found that the flow circulation intensifies as we move from 25% of the chord to 37.5%, and finally at 50% separation does not exist any more. Therefore, it could be concluded that the zone of separation is approximately between 25% and 40% of chord length. Interestingly at 30 km/hr speed, the zone of separation was nearly from 25% to 55% of chord length. However, for 40 km/hr, this zone has reduced to nearly 40% of chord length, instead of 55% while the beginning of separation remains the same. And at this speed, the sluggishness of boundary layer near the trailing edge that was observed in the case of 30 km/hr speed, has also reduced significantly. The reason is that as the separation zone reduces, its slow-downing effect on boundary layer also decreases and hence sluggishness of the boundary layer at the trailing portion also decreases.

6.2.3 Velocity profiles on the lower surface of the wing

On the lower surface of the wing, velocity profiles are examined at five chord-wise stations along with the flow directions. Figures 6.2.3(i) to 6.2.3(v) and 6.2.3(vi) to 6.2.3(ix) represent the velocity profiles for U_∞= 30 km/hr and U_∞= 40 km/hr respectively at different stations.

Analyzing the graphs, it is sees that on the lower surface of the aerofoil, there is no separation. However, at the trailing edge of the wing, there are evidences of wake formation. Again, for both speeds, the nature of boundary layers i.e. the velocity profiles are quite similar.

6.3. Velocity Profiles over the Fuselage

Like the wing, at first the nature of the boundary layer and wake formation and separation on the upper surface of the wing is studied. Investigations were done at two wind speeds, viz 30 km/hr and 40 km/hr (subsection 6.3.1 and 6.3.2 respectively). Again, the same investigations were done for the lower surface of wing at the two speeds (subsection 6.3.3). Yaw meter probes were set at appropriate position and the corresponding spring deflections given by the pressure transducer were recorded in a computer, speeds and flow angles calculated.

In this section velocity profiles on both the upper and lower surfaces of the fuselage are presented and its characteristic features analysed for better understanding of the flow field in the region. Profiles for velocities U_∞= 30 km/hr and U_∞ = 40 km/hr are presented separately.

6.3.1 Velocity Profiles on the upper surface of the fuselage at U_∞= 30 km/hr

For different position along the chord of the wing, velocity profiles are found out by positioning the probes at different vertical distances from the surface. From the readings of the three probes of yaw meter, the flow angles are also calculated. For different positions along chord, velocities and flow angles at different vertical distances are given in the table **6.3.1(i)** to **6.3.1(x)**. With the help of the table corresponding graphs are plotted.

From the curves, it is seen that at 30 km/hr speed over the wing, separation begins nearly at 25% of chord from the leading edge (figure 6.3.1(ii)) and continues till 50% of the chord (figure 6.3.1 (v)). It is found that the separation intensifies as we move from 35% of the chord to 55%, and finally at 62.5% separation does not exist any more. Therefore, it can be concluded that the zone of separation is approximately between 35% and 60% of chord. Comparing this with the same phenomenon of the wing, which is a same aerofoil with 1/3 chord length, we find that there is a delay in separation while the length of separation zone in terms of percentage of chord length is almost same. Also, here we find an increase in the depth of separation, which is nearly at the same scale as that of the geometries between wing and fuselage. Therefore, similarity principles become evident. Finally, like the wing, here too, the boundary layer becomes sluggish near the trailing edge, which may also be due to the separation.

6.3.2 Velocity Profiles on the upper surface of the fuselage at U_∞= 40 km/hr

Now, the wind speed is set at 40 km/hr with help of variable frequency drive. For different position along the chord of the wing, here too, velocity profiles are found out by positioning the probes at different vertical distances from the surface. From the readings of the three probes of yaw meter, the flow angles are also calculated. For different positions along chord, velocities and flow angles at different vertical distances are given in the table 6.3.2(i) to 6.3.2(b)(x). With the help of the table corresponding graphs are plotted.

From the curves, it's seen that at this 40 km/hr speed over the wing, separation begins nearly at 35% of chord from the leading edge (figure 6.3.2(ii)) and continues till 45% of the chord (figure

51

6.3.2(iv)). It is found that the separation intensifies as we move from 35% of the chord to 45%, and finally at 55% separation does not exist any more. Therefore, it can be concluded that the zone of separation is approximately between 35% and 45% of chord. Interestingly, at 30 km/hr speed, the zone of separation was nearly from 35% to 55% of chord. However, for 40 km/hr, this zone has reduced to nearly 45% of chord, instead of 55% while the beginning of separation remains the same. Comparing this with the same phenomenon of the wing, which is a same aerofoil with 1/3 chord length, we find that there is a delay in separation while the length of separation zone in terms of percentage of chord length is almost same. Also, here we find an increase in the depth of separation, which is nearly at the same scale as that of the geometries between wing and fuselage. Therefore, similarity principles become evident. And at this speed, the sluggishness of boundary layer near the trailing edge that was observed in the case of 30 km/hr speed, has also reduced significantly. The reason is that as the separation zone reduces, its slow-downing effect on boundary layer also decreases and hence sluggishness of the boundary layer at the trailing portion also decreases.

6.3.3 Velocity profiles on the lower surface of the fuselage

Under the lower surface of the fuselage, velocity profiles were examined at six chord-wise stations along with the flow angles. Figures 6.3.3(i) to 6.3.3(vi) and 6.3.3(vii) to 6.3.3(xii) represent the velocity profiles for U_∞= 30 km/hr and U_∞= 40 km/hr respectively at different stations.

Analyzing the graphs, we see that under the lower surface of the aerofoil, there is no separation. However, at the trailing edge of the wing, there are evidences of wake formation, the intensity of which is observed to be greater in case of fuselage than in the case of the wing. Again, for both speeds, the nature of boundary layers i.e. the velocity profiles are quite similar.

6.4 Velocity Profiles over upper surface of wing at curved portion

In this project the model with aerofoil fuselage has slightly been modified following the design of MIG-29 fighter plane. Hence, we were interested to see any difference between the boundary layer at the curved portion of the wing and that at the center of the wing, which is a pure NACA 2412 aerofoil. Figures 6.4.1(i) to 6.4.1(x) and 6.4.2(i) to 6.4.2(x) represent the velocity profiles on the upper surface of the wing at the curved portion for U_∞= 30 km/hr and U_∞= 40 km/hr respectively at different stations. Here the flow filed is much alike that at the center of the wing. The separation region too have the same characteristics like at the centre of the wing.

6.5 Vector Diagrams

Vector diagrams of the flow filed are helpful in having a better picture of the flow characteristics. Therefore, vector diagrams are drawn for both the wing and the fuselage for both the speeds.

Figure 6.5(i) presents the vector digram of the flow field over the wing at a speed of 30 km/hr. To obtain a better picture of the flow near the wall as well as to see the observe the separation region closely, a vector diagram is drawn with taking only the first five sets of data and presented in figure 6.5(ii).

Figure 6.5(iii) and figure 6.5(iv) present of vector diagrams of flow over the wing at 40 km/hr speed, with the complete data set and first five sets, respectively.

Figure 6.5(iv) and figure 6.5(v) show vector diagrams over the fuselage at 30 km/hr and similar digrams are shown for 40 km/hr speed over fuselage in figure 6.5(vi) and figure 6.5(viii).

6.6 Analysis of negative pressure zone

Figure 6.6 (i) and figure 6.6 (ii) show the pressure distribution in the negative pressure zone of the wing, for 30 km/hr and 40 km/hr speed respectively.

Figure 6.6 (iii) and figure 6.6 (iv) present the pressure distribution in the negative pressure zone of the fuselage, for 30 km/hr and 40 km/hr speed respectively.

The separation zone over the wing at its center, over the wing at the curved portion and over fuselage are plotted against percentage of chord length and shown figure 6.6(v), figure 6.6(vi) and figure 6.6(vii) respectively.

6.7 Growth of Boundary Layer

Growth of boundary layer over the wing and the fuselage are presented in figure 6.7(i) and figure 6.7(ii) respectively. It is seen that the boundary layer thicken as we move from the leading edge to the trailing edge of the aerofoil. We also see that for lower speeds, the boundary layer is thicker than that for higher speeds.

Curves
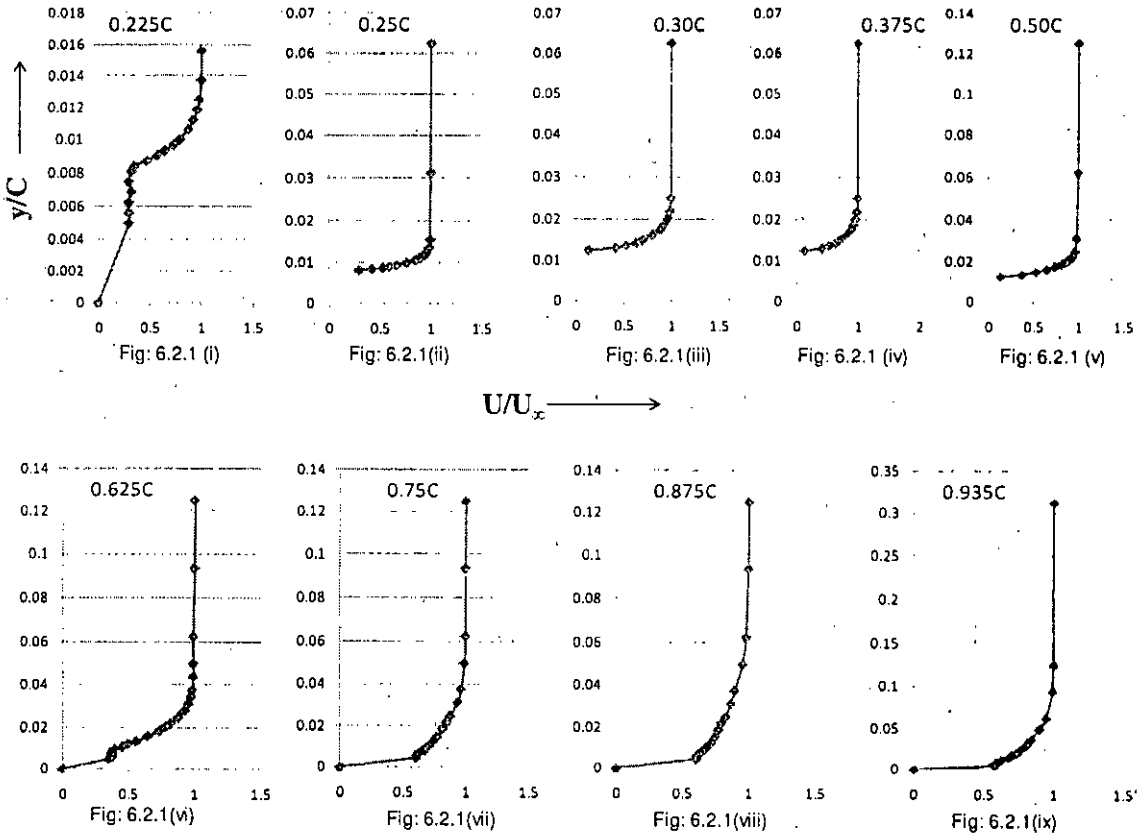
Figure- 6.2.1: Velocity profiles over the upper surface of the wing at 30 Km/hr speed
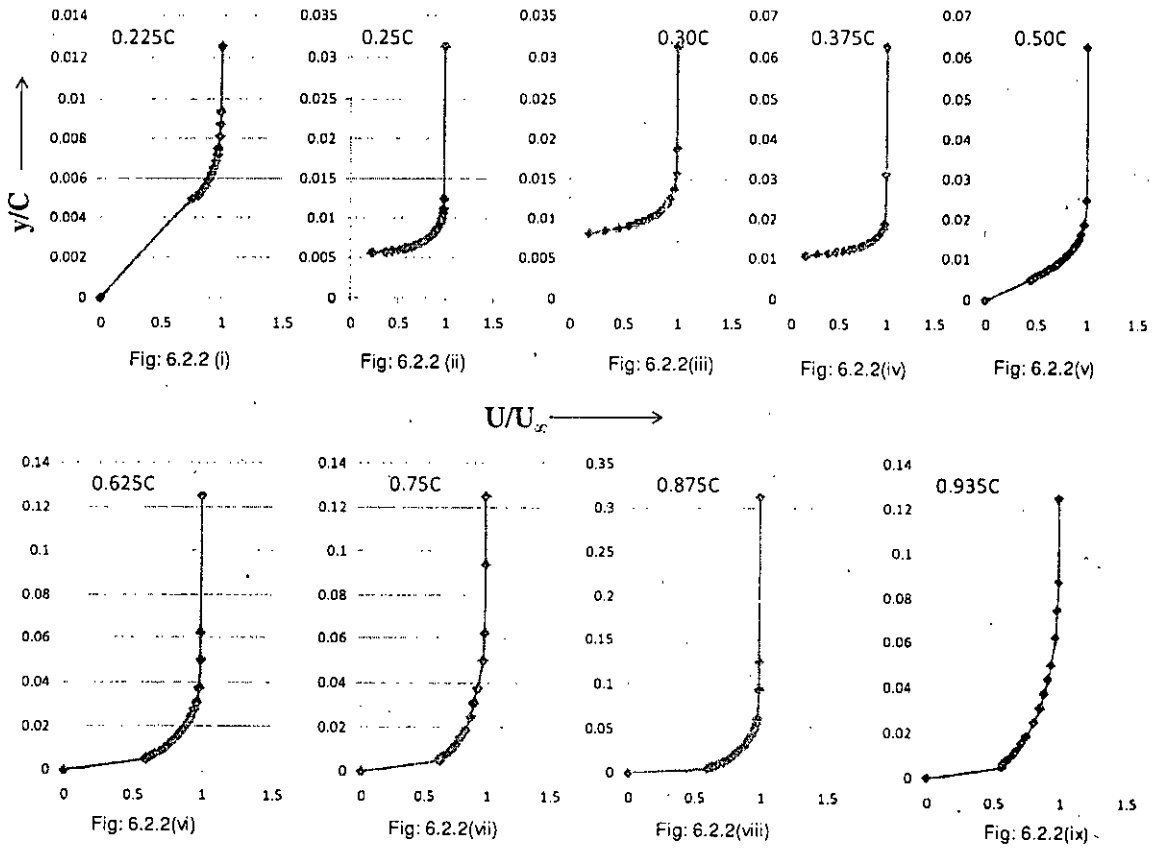
Figure- 6.2.2: Velocity profiles over the upper surface of the wing at 40 Km/hr speed
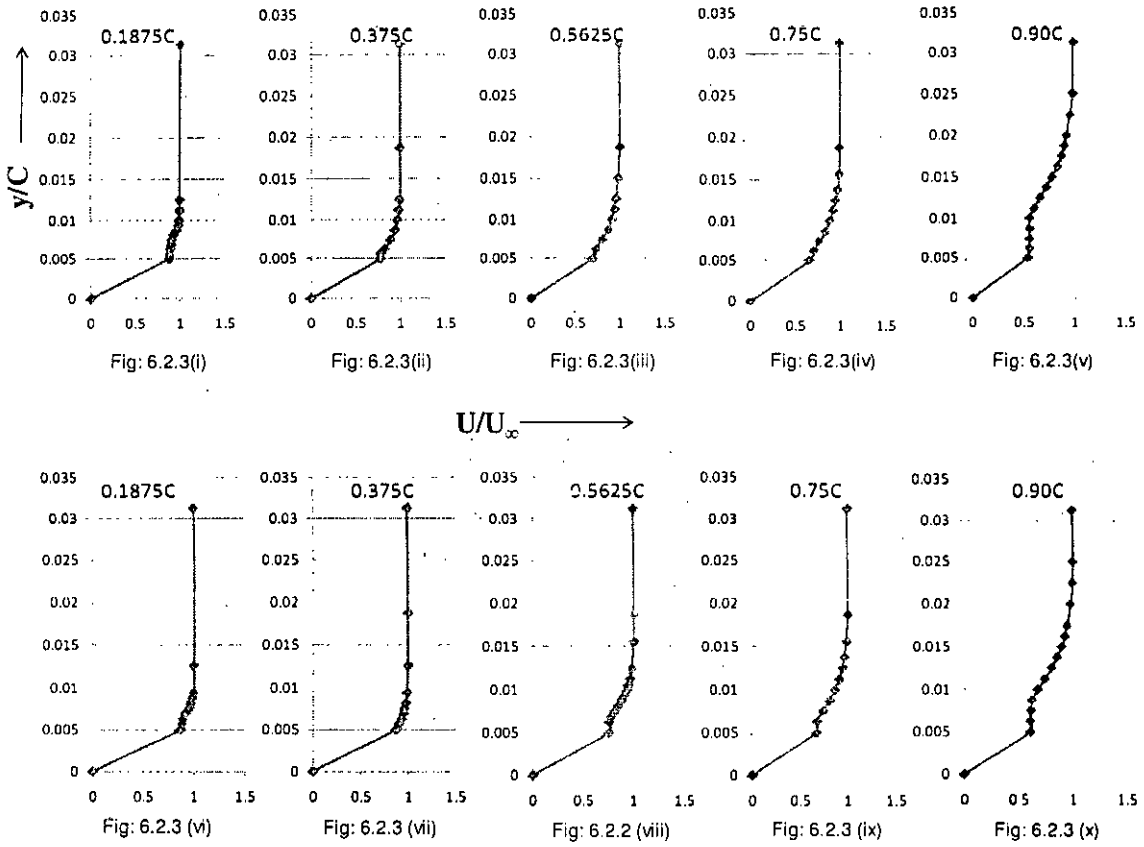
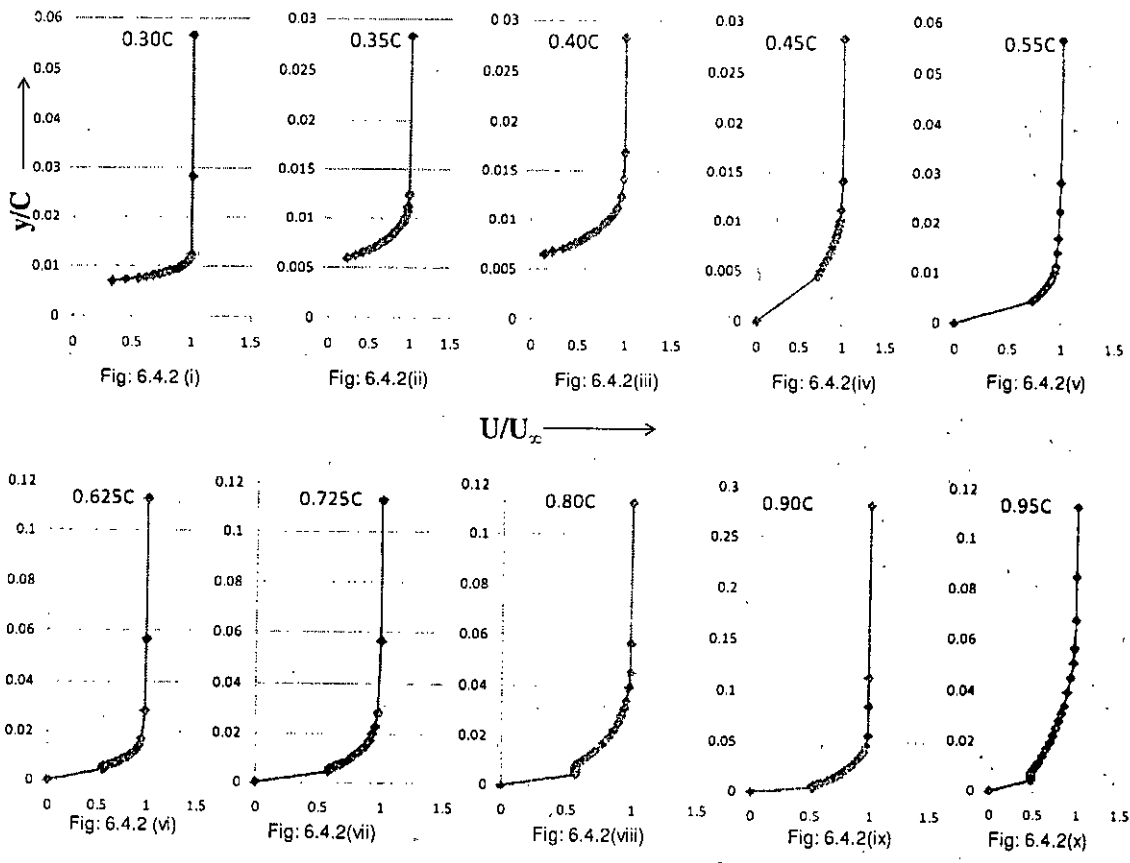**Figure- 6.2.3:** Velocity profiles over the lower surface of the wing

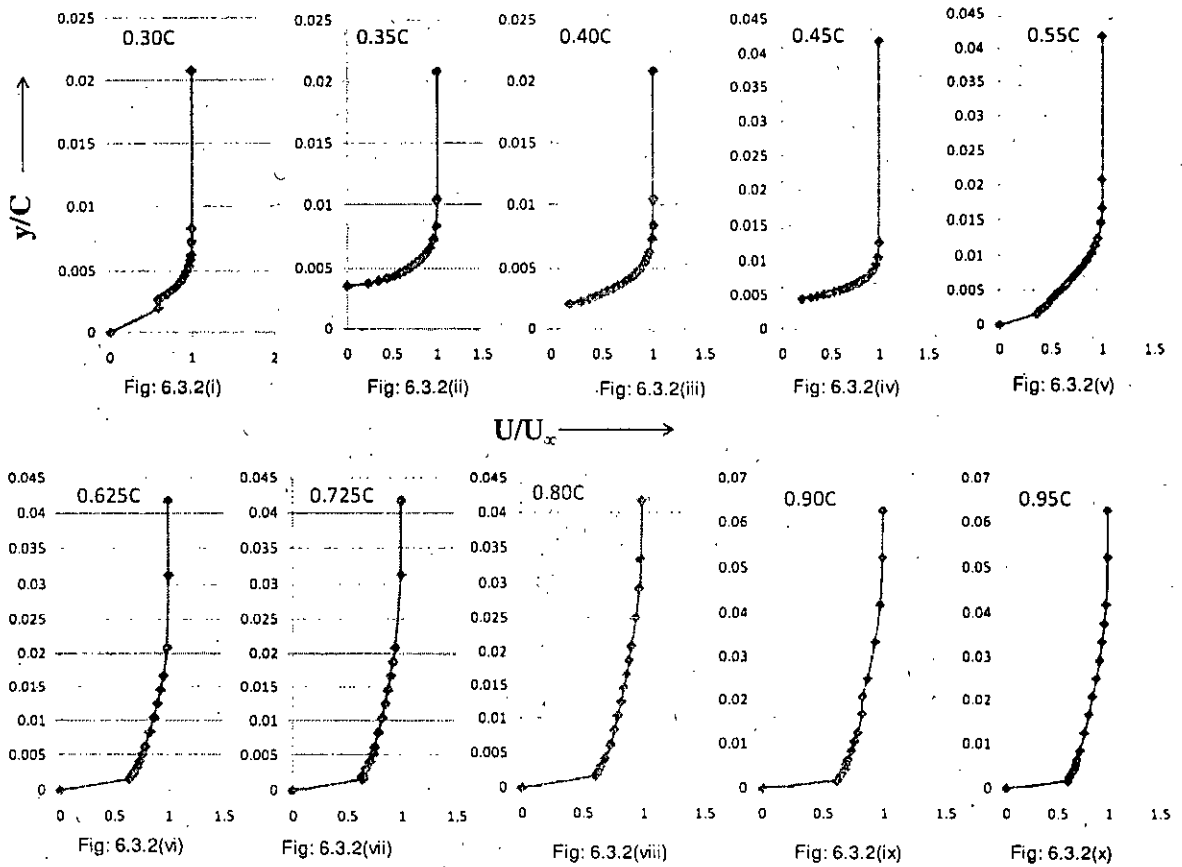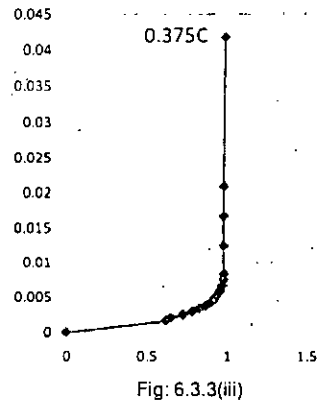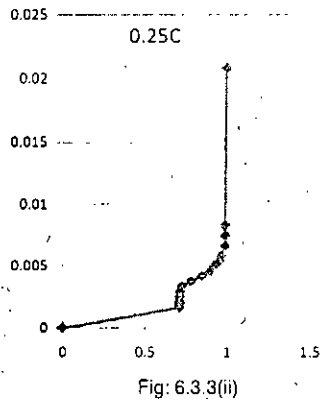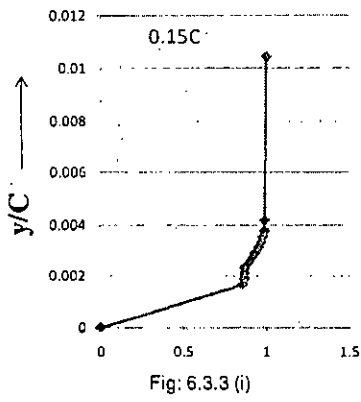Figure- 6.3.1: Velocity profiles over the upper surface of the fuselage at 30 Km/hr speed

Figure- 6.3.2: Velocity profiles over the upper surface of the fuselage at 40 Km/hr speed
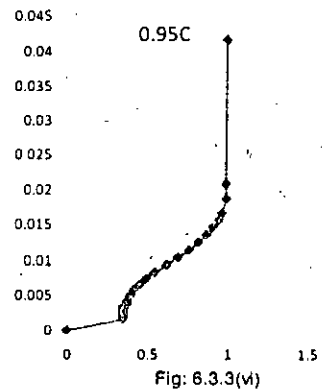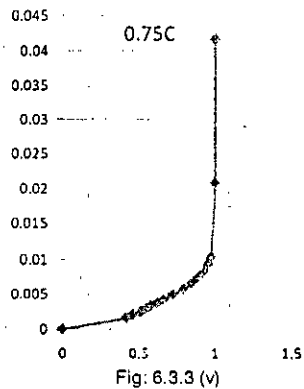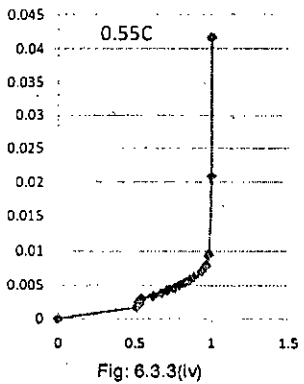
Figure- 6.3.3: Velocity profiles over the lower surface of the fuselage at 30 Km/hr speed
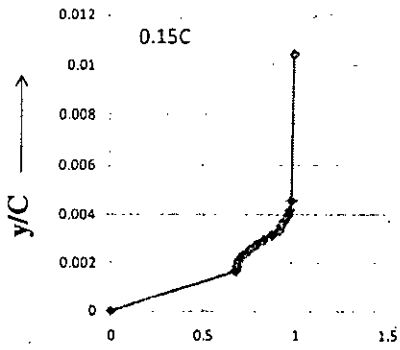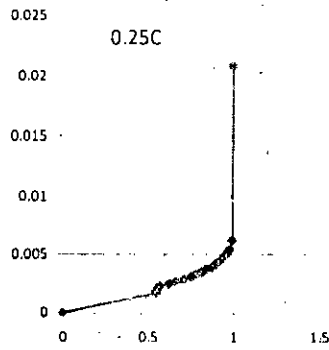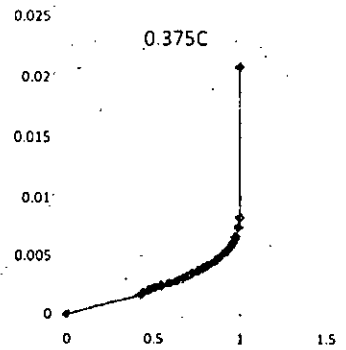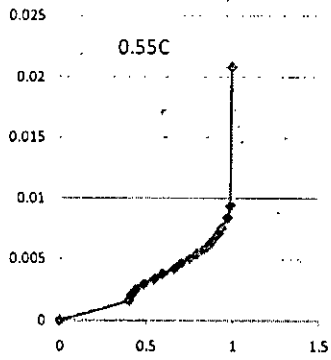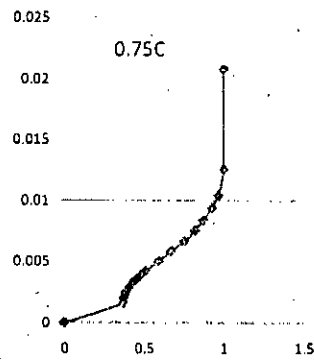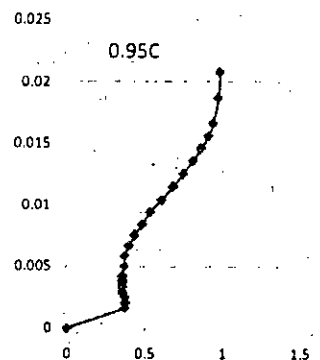
Figure- 6.3.3: Velocity profiles over the lower surface of the fuselage at 40 Km/hr speed
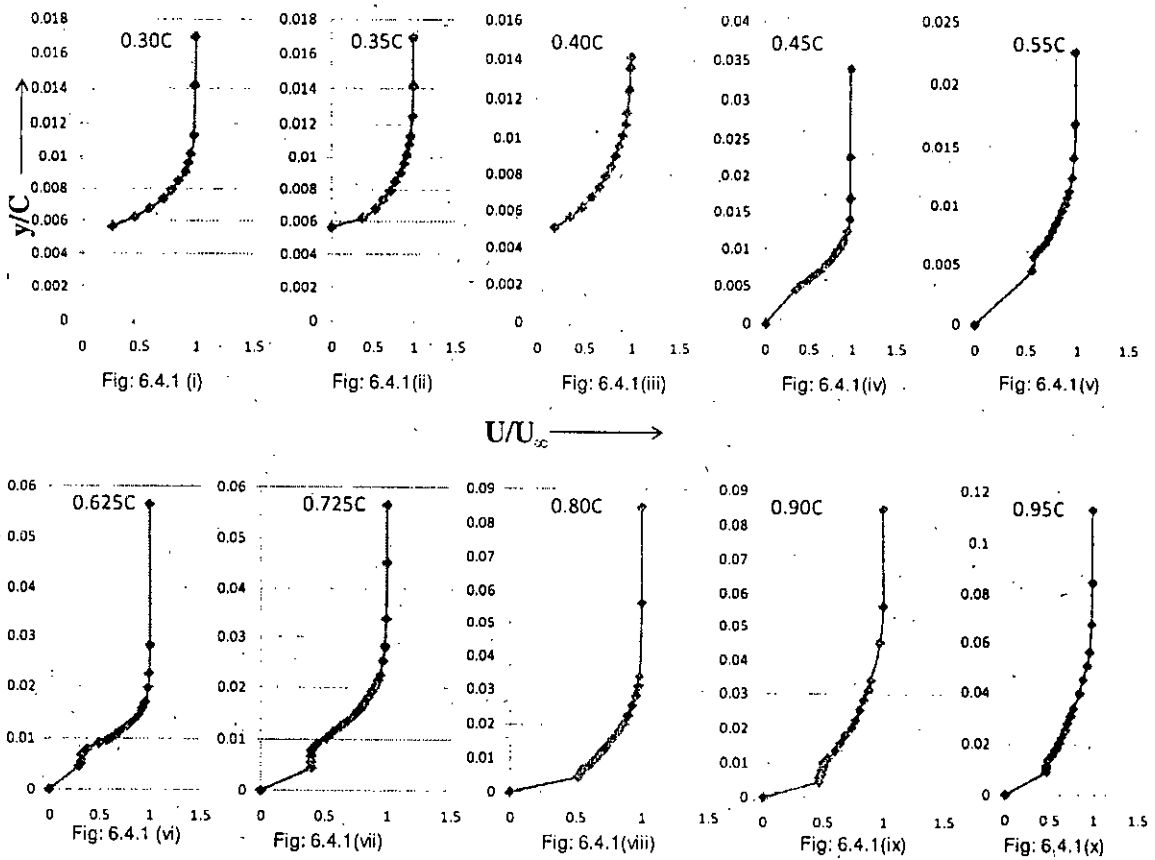
Figure- 6.4.1: Velocity profiles over the upper surface of the wing at the curved section at 30 Km/hr speed
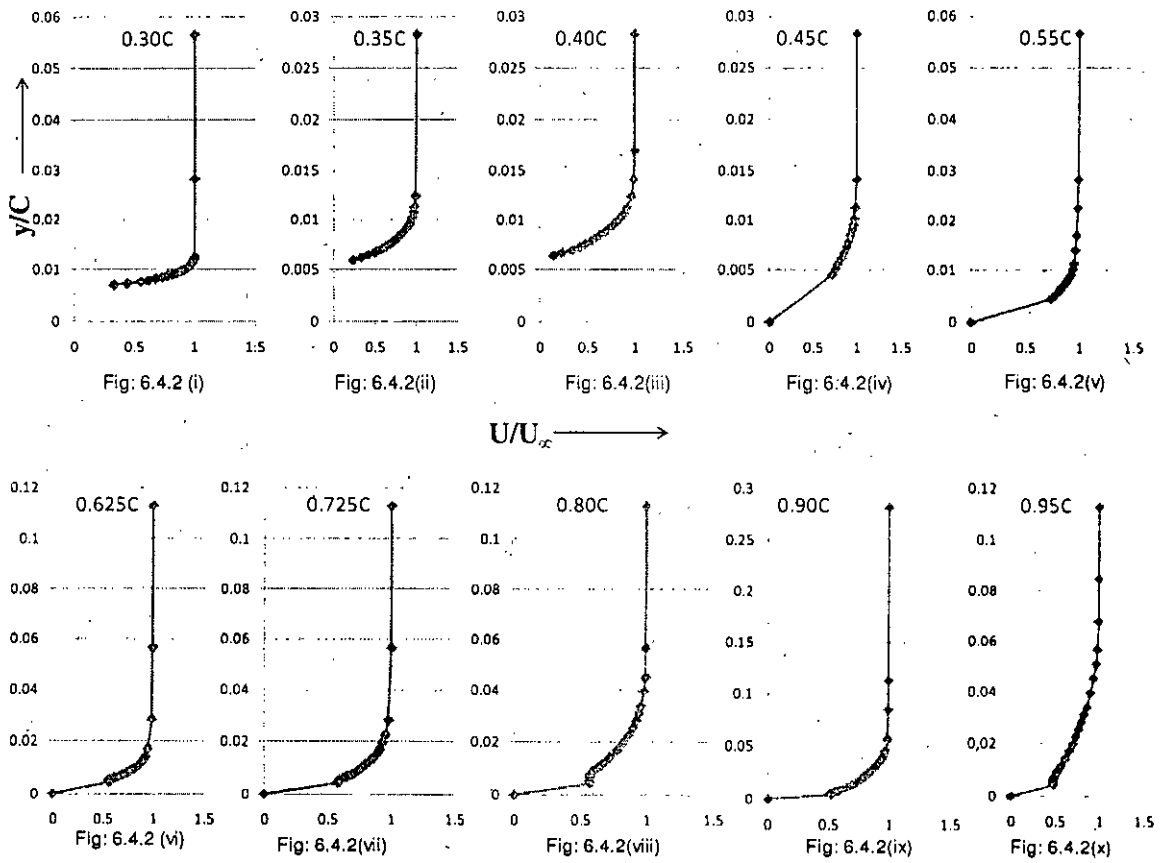
Figure- 6.4.2: Velocity profiles over the upper surface of the wing at the curved section at 40 Km/hr speed

63
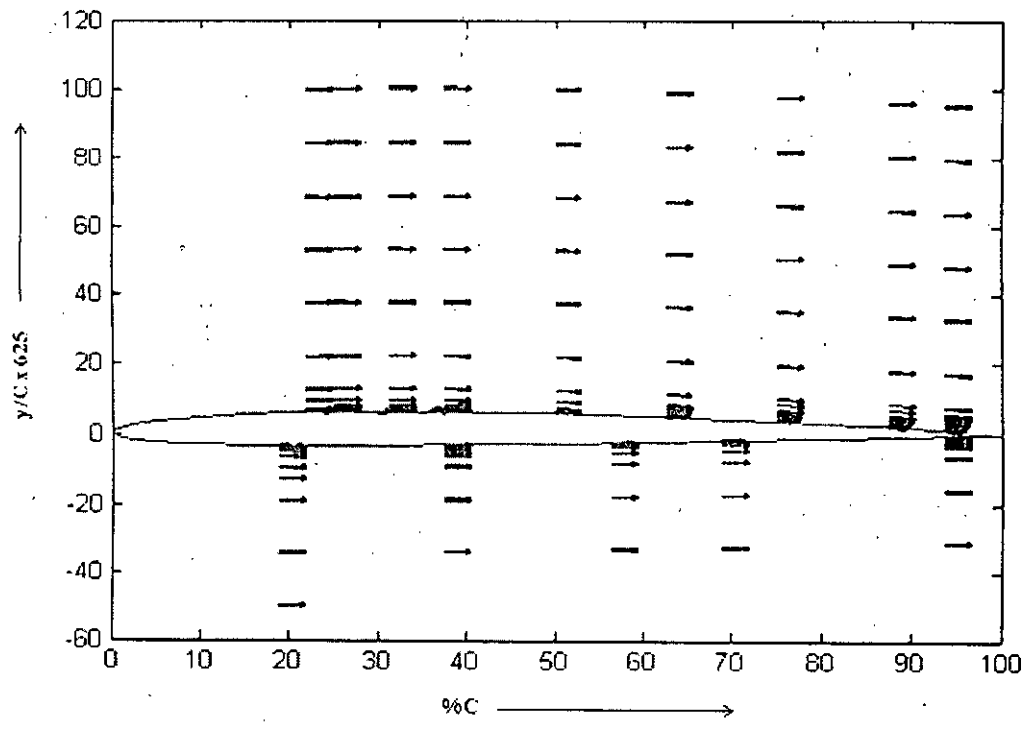
Figure- 6.5(iii) : Vector diagram of flow field over the wing aerofoil at 30 Km/hr speed: complete view
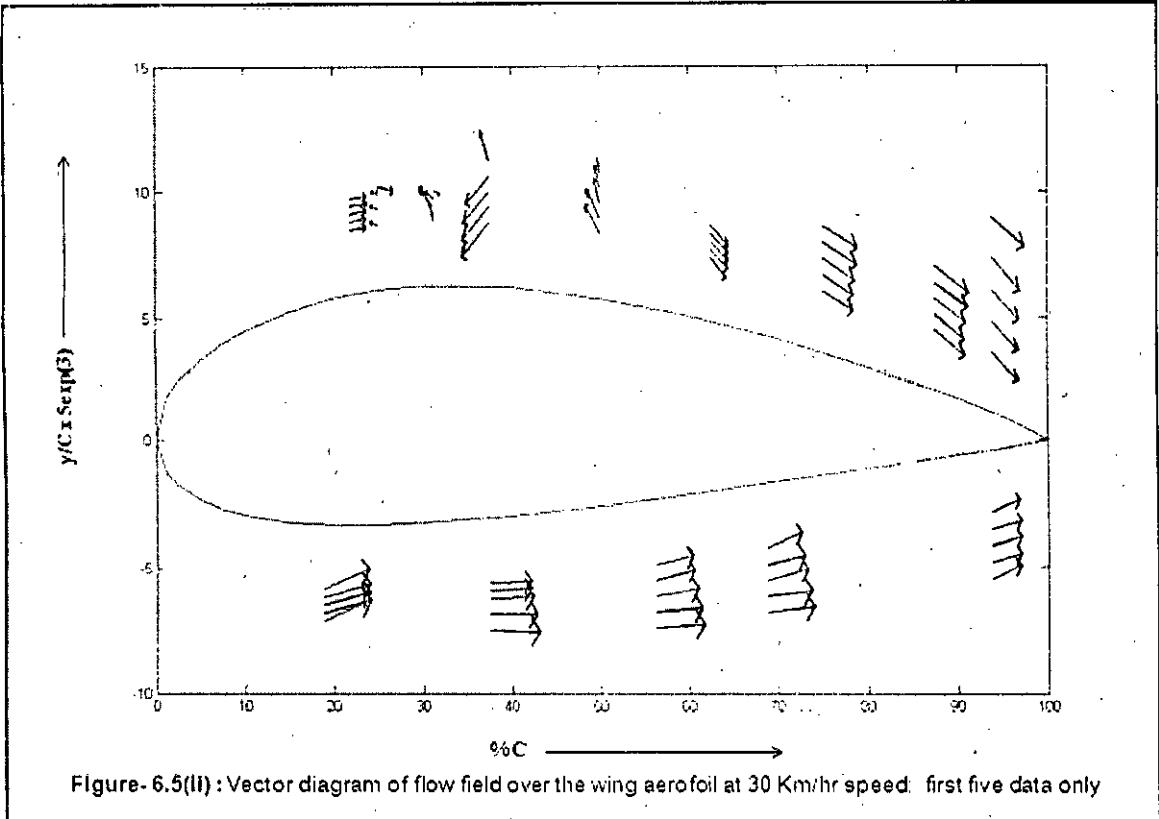
Figure- 6.5(ii) : Vector diagram of flow field over the wing aerofoil at 30 Km/hr speed: first five data only
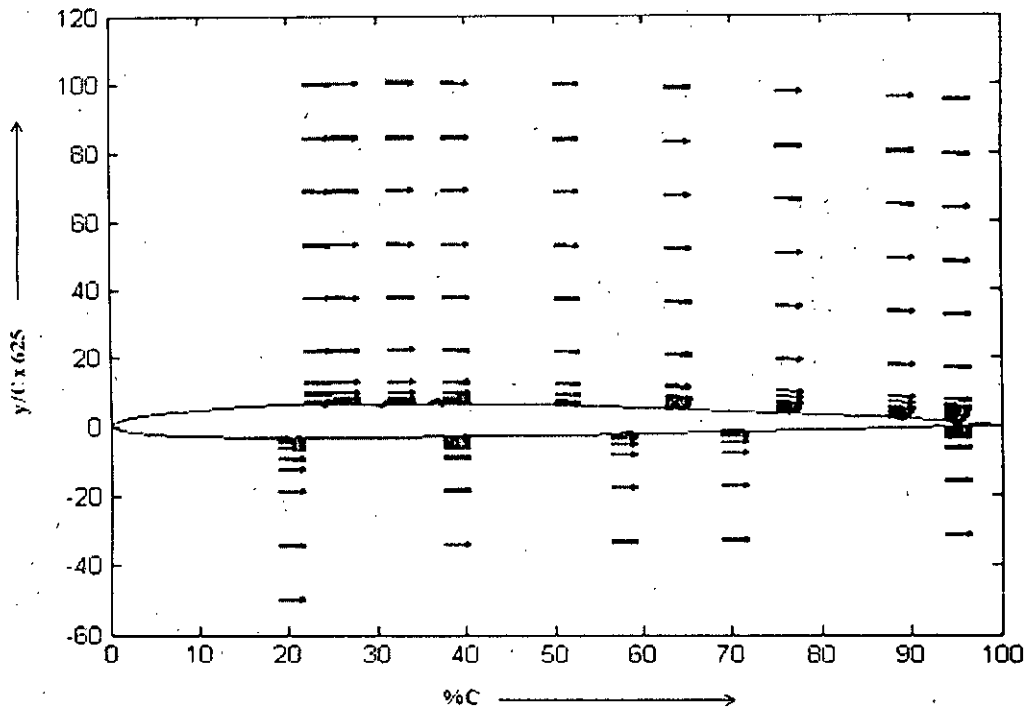
Figure- 6.5(iii) : Vector diagram of flow field over the wing aerofoil at 40 Km/hr speed complete view
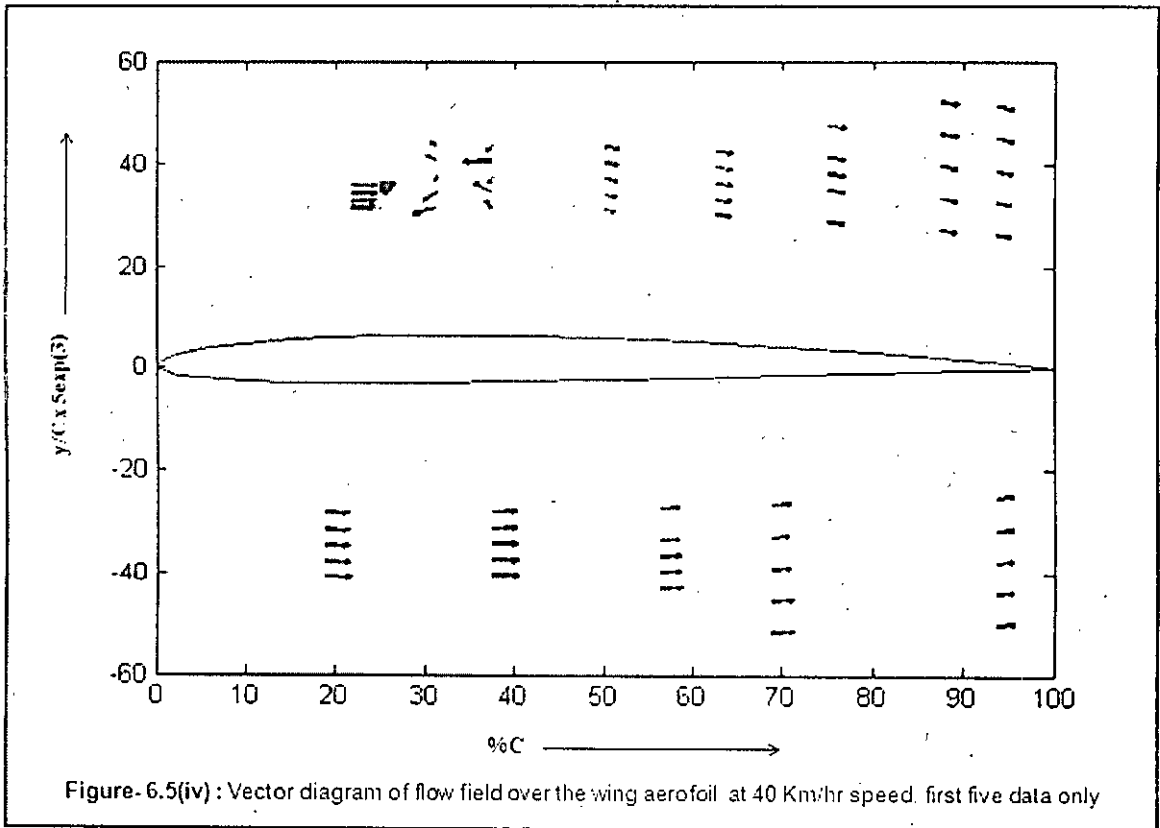
Figure- 6.5(iv) : Vector diagram of flow field over the wing aerofoil at 40 Km/hr speed, first five data only
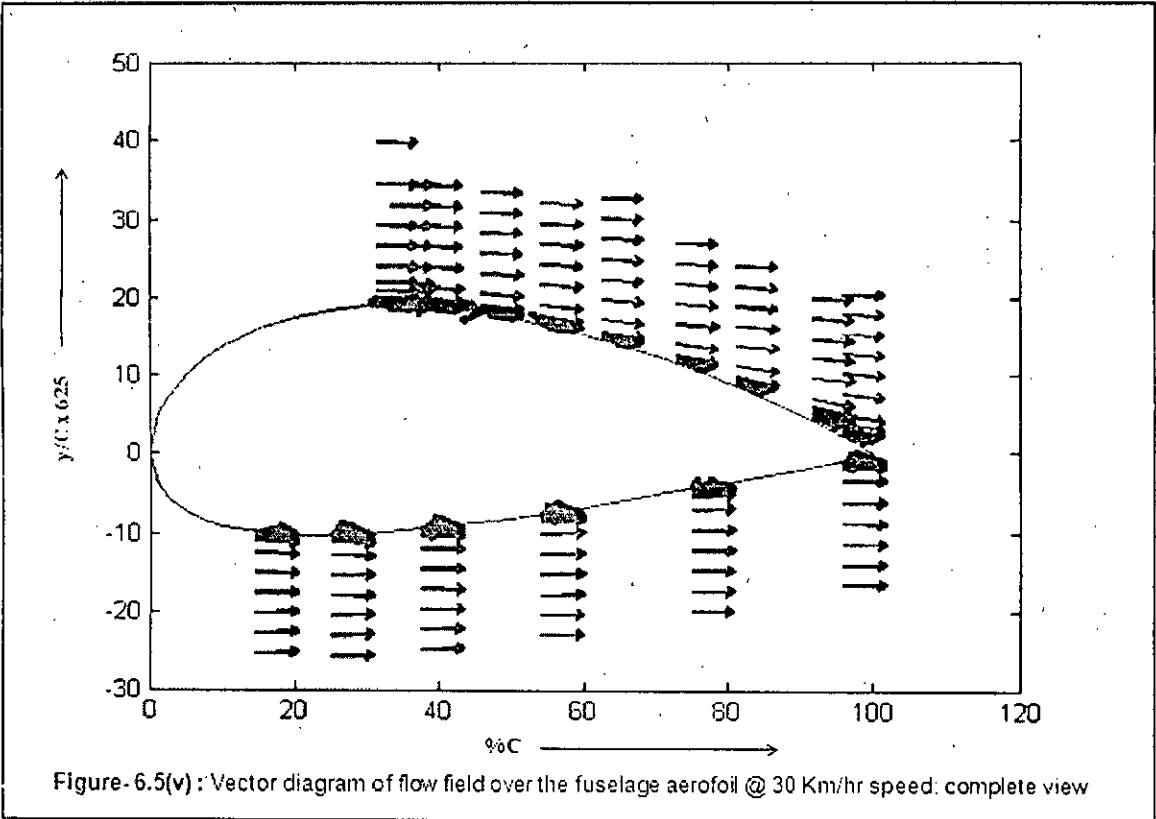
Figure- 6.5(v) : Vector diagram of flow field over the fuselage aerofoil @ 30 Km/hr speed: complete view
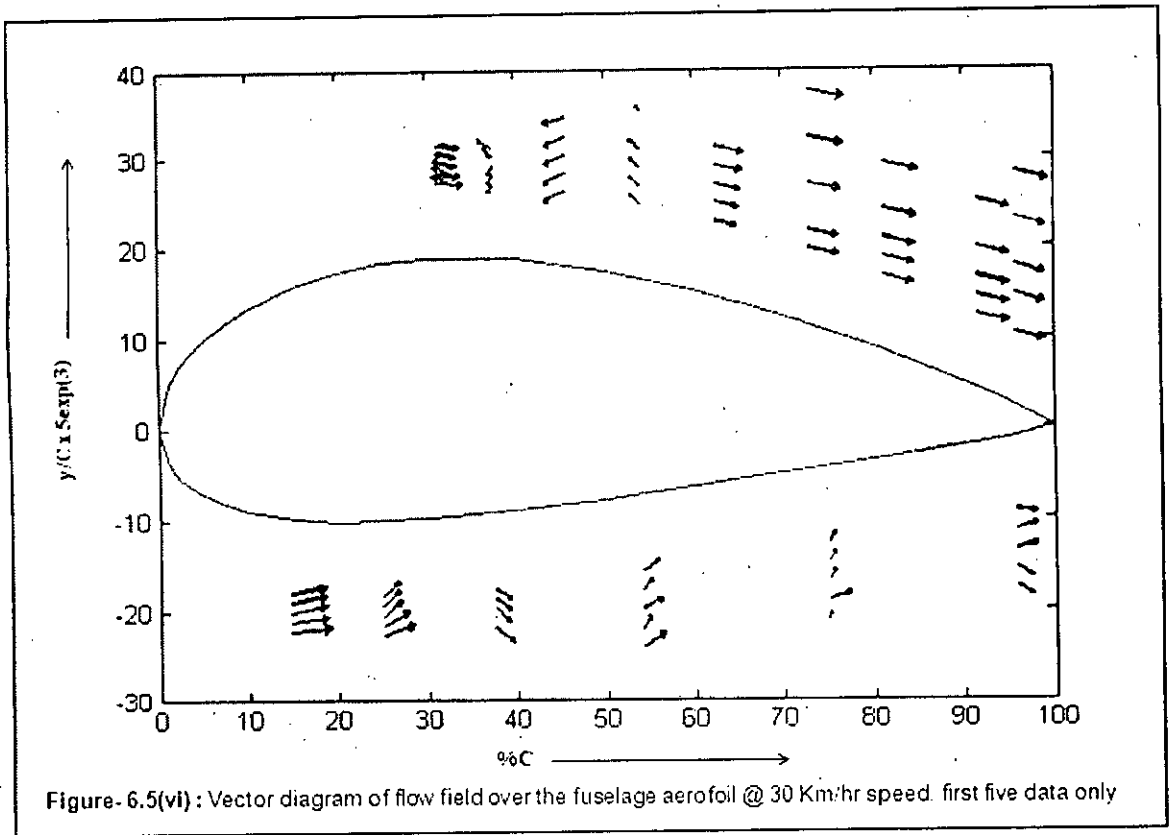
Figure- 6.5(vi) : Vector diagram of flow field over the fuselage aerofoil @ 30 Km/hr speed. first five data only

69
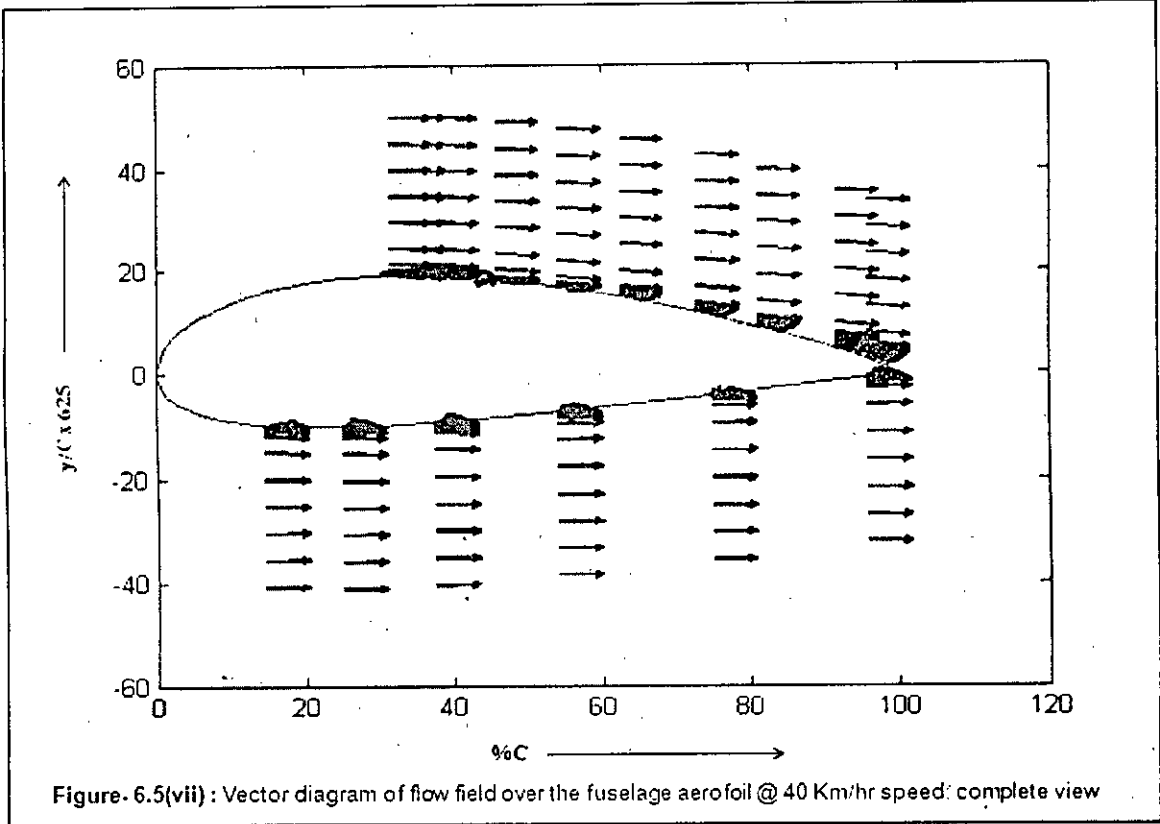
Figure- 6.5(vii) : Vector diagram of flow field over the fuselage aerofoil @ 40 Km/hr speed: complete view
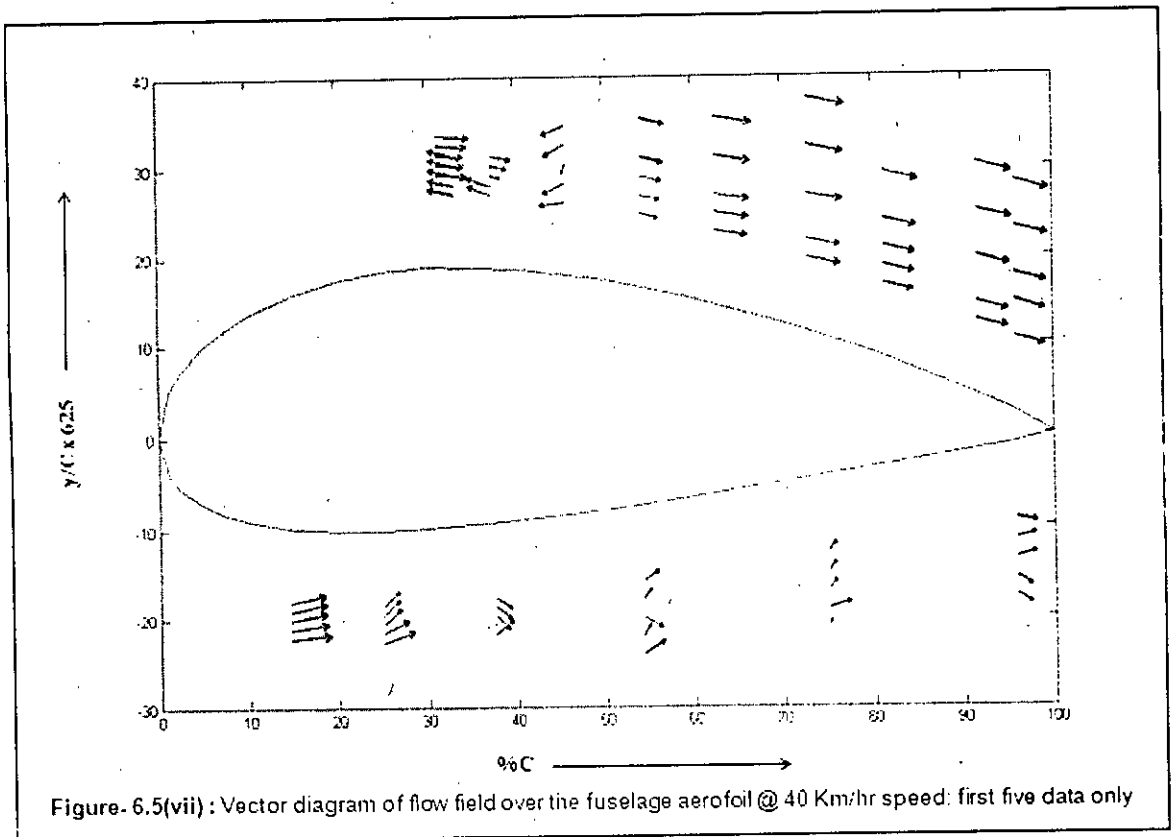
Figure- 6.5(vii) : Vector diagram of flow field over the fuselage aerofoil @ 40 Km/hr speed: first five data only

Figure- 6.6(i) : Pressure distribution over the wing in the separation zone at 30 Km/hr Speed

Figure- 6.6(ii) : Pressure distribution over the wing in the separation zone at 40 Km/hr Speed

Figure- 6.6(iii) : Pressure distribution over the fuselage in the separation zone at 30 Km/hr Speed

Figure- 6.6(iv) : Pressure distribution over the fuselage in the separation zone at 30 Km/hr Speed
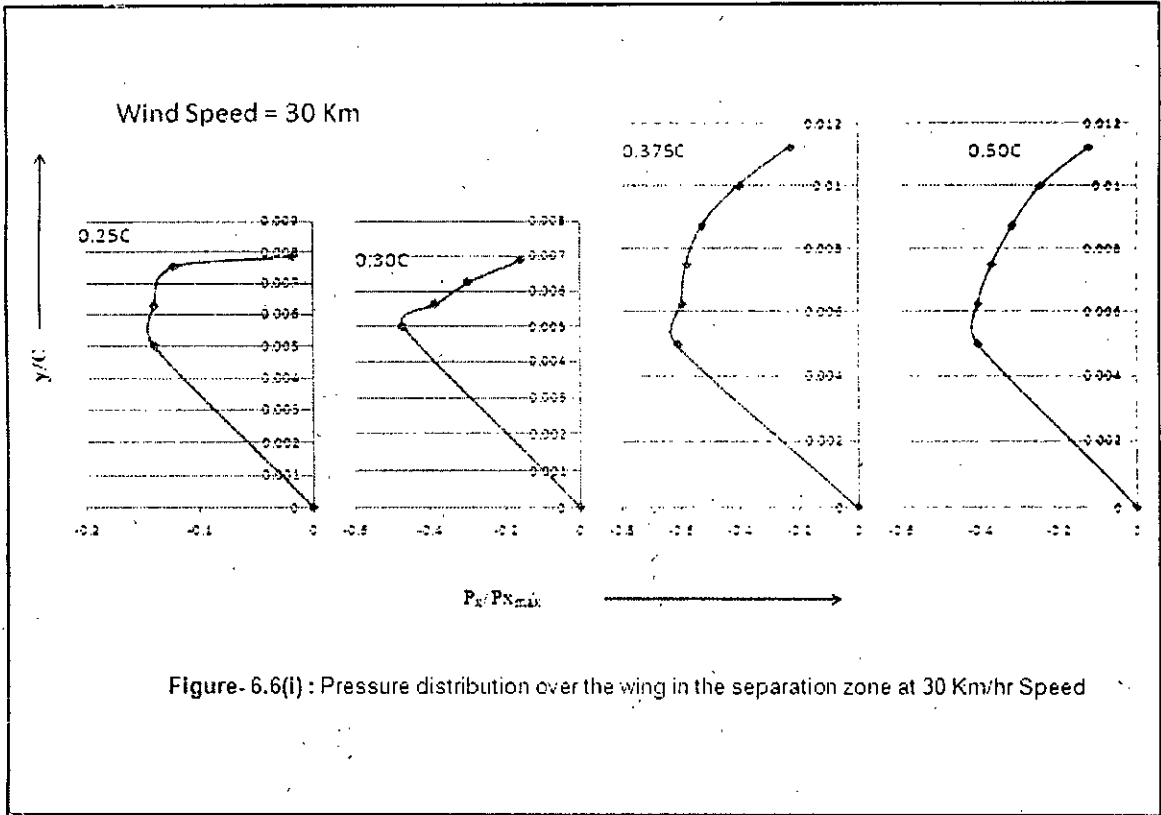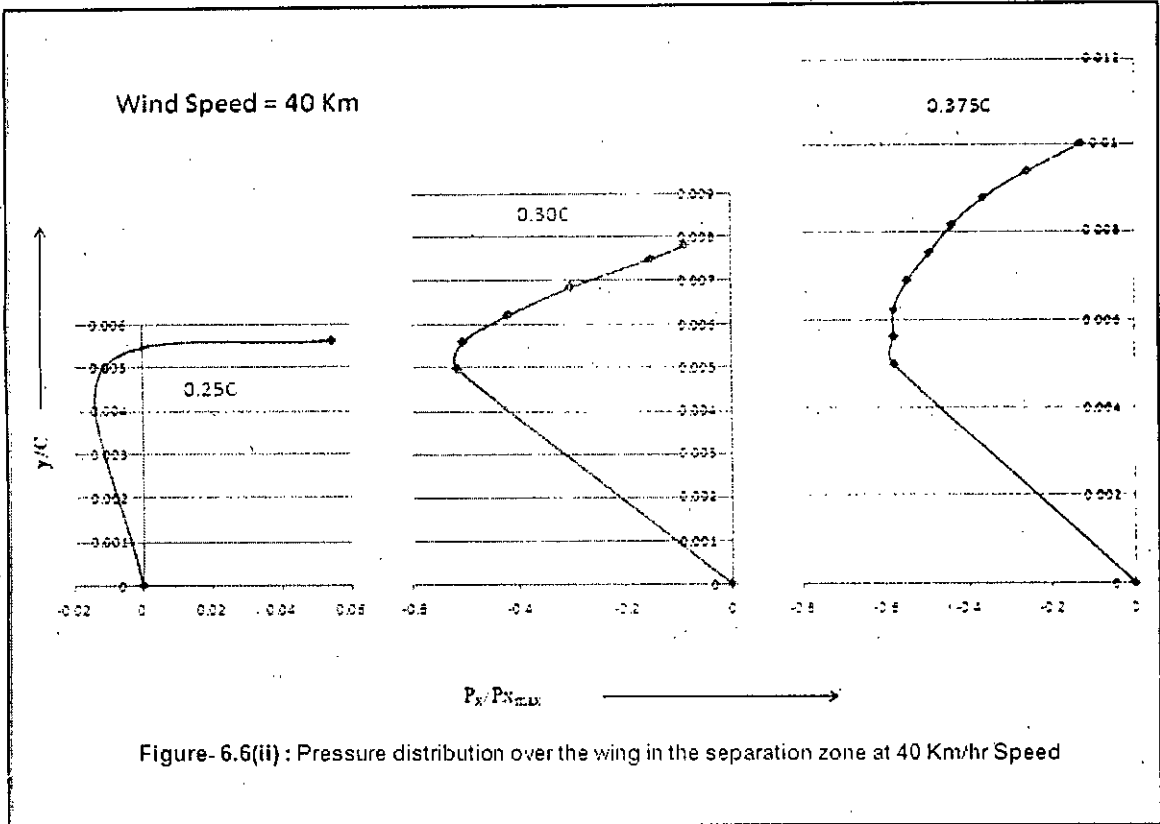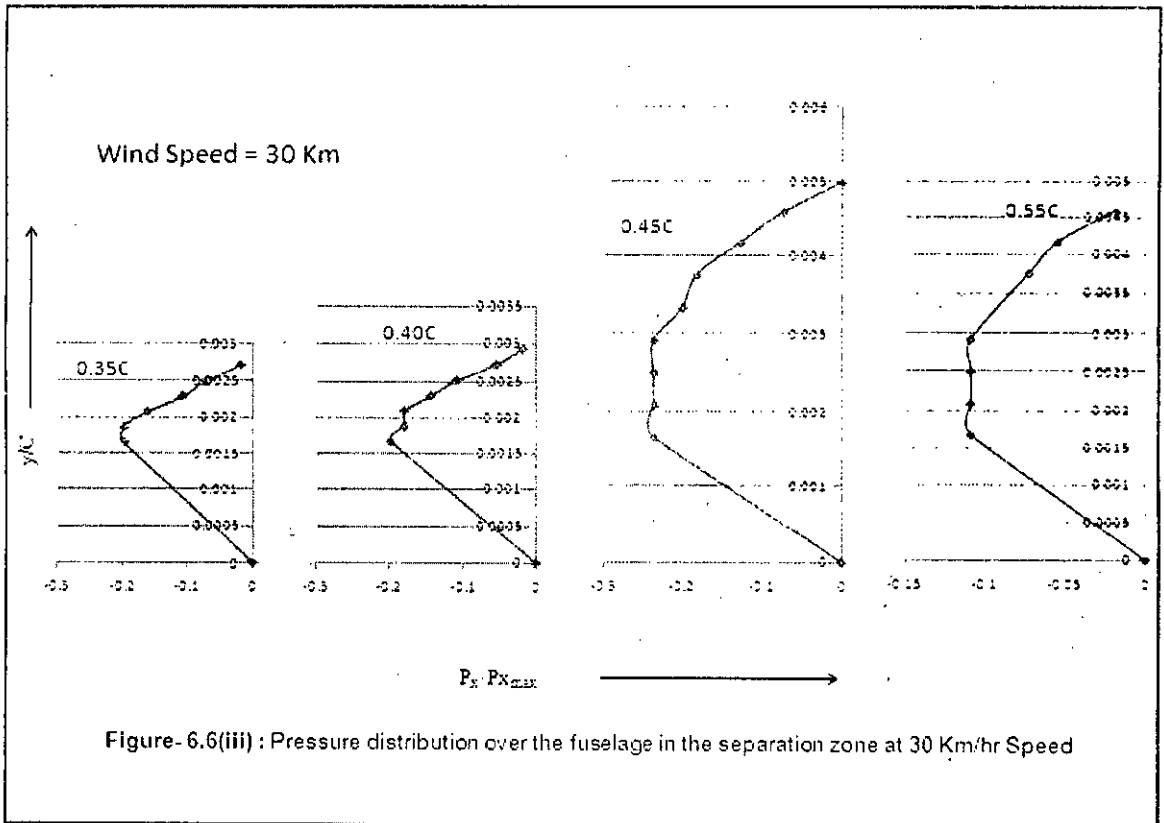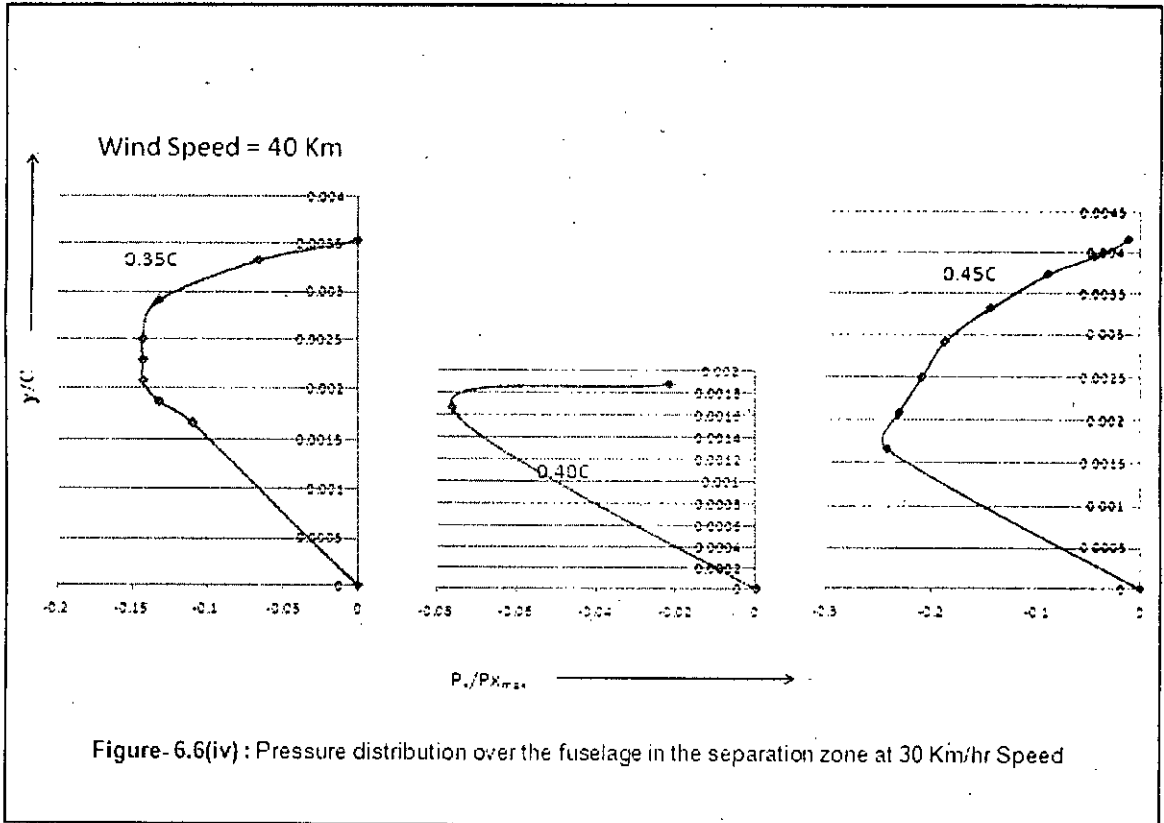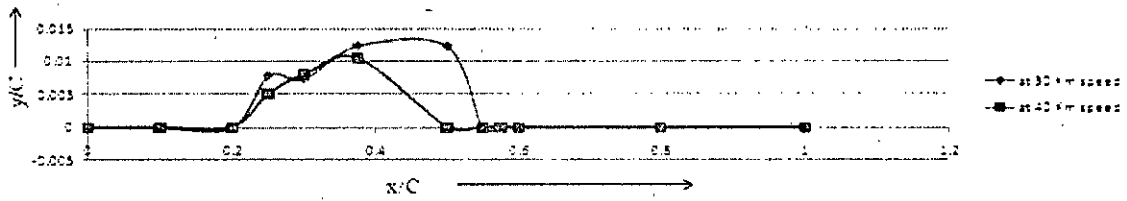
Figure- 6.6(v) : Negative pressure zone over the wing
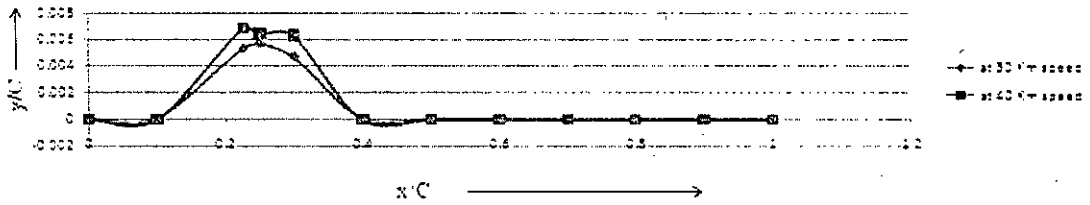
Figure- 6.6(vi) : Negative pressure zone over the curved portion of the wing
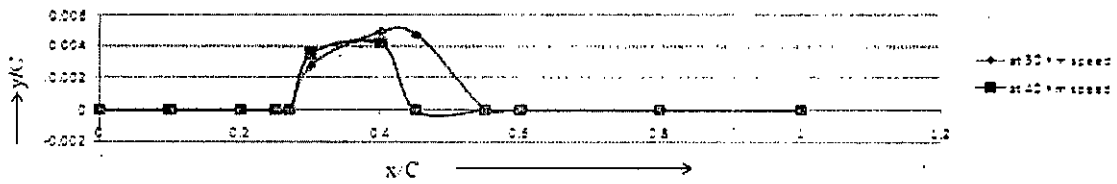
Figure- 6.6(vii) : Negative pressure zone over fuselage

Figure-6.7(i) : Growth of boundary layer over the wing

Figure-6.7(ii) : Growth of boundary layer over the fuselage

77
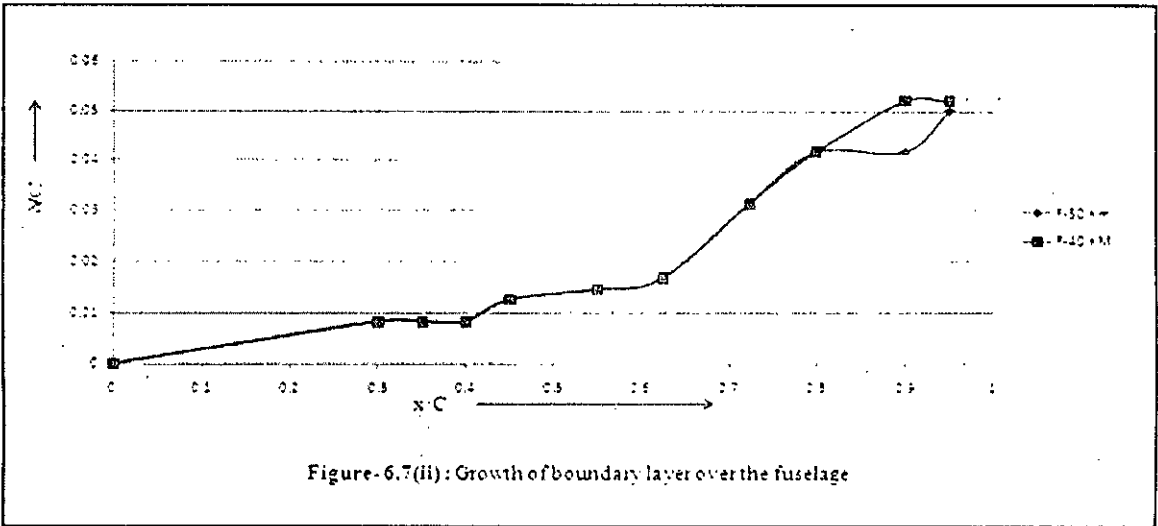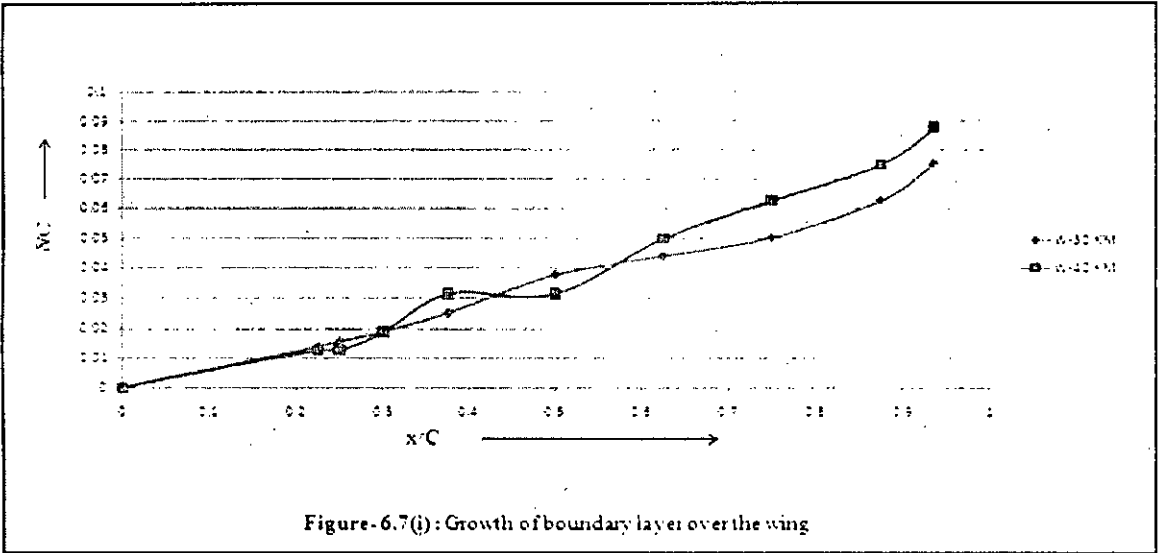
Chapter 7

CONCLUSIONS AND RECOMENDATIONS

7.1. Conclusions:

In the present investigation, both general and specific characteristics of flow pattern are observed.

General Observations:

1. From the analysis of the velocity profiles on the upper and lower surface of the wing and fuselage, it is found that separation occurs only on the upper surface of the aerofoils.

2. Analysis of the velocity profiles over the wing for 30 km/hr and 40 km/hr speeds show that the separation zone shrinks at 40 km/hr speed for both the wing and fuselage. The dept of separation zone also reduces, by very small percentage though, for 40 km/hr speed for both aerofoils.

3. Comparing the velocity profiles on the wing and the fuselage at the same speed, it is found that the separation zone shifts backward in the case of the fuselage, which is the same arofoil like the wing, but has a chord length three times of that of the wing.

4. The growth of boundary layer over the aerofoils are not found to be asymptotic as the case is for flat plates. Growth of boundary layer over the wing shows a linear tendency while over the fuselage, the tendency is not that linear.

Specific Observations:

1. The design modification at the wing-fuselage interface, which was done in accordance with the design of MIG-29 fighter plane, seems to have good impact on separation phenomenon, as the region shrinks over the modified zone.

2. At the trailing portion of each aerofoil, there are evidences of wake formation. Hence, vortex generators as described in section 2.6 may have good impact on aerodynamic performance. Similarly, to control separation suction and/or discharge boundary layer control technique can be adopted for prototypes.

7.2. Recommendations

1. This research work focuses on the two dimensional flow characteristics over the wing and the fuselage. However, the flow is assumed to be three dimensional around the interface regions and at the wing tips, if not at other points too. Therefore, a study of the three dimensional flow would give a complete picture of the flow field.

2. Flaps and ailerons improve the controlling and maneuvering capability of an airplane. So flaps can be introduced in the aerofoiled fuselage to show their effect on the overall stability of the model plane.

3. Winglets are not used in the model over which flow characteristics is studied in this research. The impact of winglets on the flow characteristics can be studied by using a wingletted model. Winglets can be designed with the help of computational a software (e.g., FLUENT, ANSYS CFX) to ensure aerodynamic winglets that would provide a good reduction of the induced drags.

4. Blended Wing Body (BWB) concepts are frequently being considered in modern aircraft designs. In this research the birds body shapes are considered as aerofoiled shapes but their body shapes are also an example of BWB. So a comparison between Circular fuselage, Aerofoiled fuselage and Blended Wing Body fuselage will be more practical.

5. Only the low-speed range is considered in this research. For a complete understanding of flow characteristics over a wide range of speed, flow characteristics in other speed ranges should also be investigated.

6. This research focuses only on the 4^{0} angle of attack, the angle of attack of highest lift to drag ratio as found by the previous researcher. All other usual angle of attack combinations should be investigated to reveal the reason behind highest lift to drag ratio at 4^{0}. This would also help to obtain relevant information about flow characteristics at other angle of attacks.

REFERENCES

1) Levy, H. and Riding, R.: "Burnelli's Lifting Fuselages." Aeroplane Monthly, Vol. 8, No.7, July 1980, pp. 348-350.

2) Levy, H.: "Burnelli Lifting Fuselage Projects." Aeroplane Monthly, Vol. 8, No. 10, Oct. 1980, pp.516-517. 6. Wood, R. M. and Bauer, S. X. S.: Flying Wings/Flying Fuselages. AIAA 2001-0311, Jan. 8-11, 2001.

3) Cantilli, E.: "Saga of the Lifting Body/Flying Wing." Flight, pp. 56-61, Fall 1996.

4) Mitchell, K. A.: "Burnelli and His Lifting-Body Transports."   American Aviation Historical Society Journal, pp. 2-19, Spring 1997.

5) Riding, R.: "Burnelli's Lifting Fuselages." Aeroplane Monthly, Vol. 8, No. 6, June 1980, pp. 329-331.

6) Wood R. M., "The Contributions of Vincent Justus Burnelli" AIAA 2003-0292, Jun. 2003.

7) Wertenson, I. F., "Investigation of the Burnelli Type Airplane" Jan. 1931.

8) Wertenson, I. F., "Investigation into the Development of the Burnelli Type Airplane" Aero Digest, March 1931.

9) Wertenson, F., "The Economical Cruising Speed of the Burnelli All-Wing Monoplane Flight" Aug. 24, 1933, pp. 854-856.

10) Klemin, A., "All-Wing Lifting Fuselage, Scientific America" April 1935.

11) Burnelli Model UB-14 14-Passenger Transport Aero Digest, August 1935.

12) Watter, M. "The Burnelli Airfoil Body. Flight" The Aircraft Engineer, Sept 26, 1935.

13) Wood, R. M. and Bauer, S. X. S. "Flying Wings/Flying Fuselages" AIAA 2001-0311, Jan. 8-11, 2001.

14) http://www1.msfc.nasa.gov/Newsroom/news/releases/2002/02-182.html, November 2002.

15) Jenkins D. R., Landis T., and Miller J., "American X-Vehicles, An Inventory—X-1 to X-50, Centennial of Flight Edition, Monographs in Aerospace" History No. 31, SP-2003-4531, June 2003.

16) Hansen J. R., Kinney J., "Taylor D. B., Prickett M., and Lee J. L., The Wind and Beyond, A Documentary Journey into the History of Aerodynamics in America" Volume II: Reinventing the Airplane June 2000.

17) Tucker V. A., "Gliding Birds: Reduction of Induced Drag by Wing Tip Slots Between the Primary Feathers" Department of Zoology, Duke University, Durham, NC 27706, USA, Accepted 5 March 1993.

18) Hummel, D. (1980), "The aerodynamic characteristics of slotted wing-tips in soaring birds." In Acta XVII Congressus Internationalis Ornithologici (ed. R. Nöhring), pp. 391–396.

19) Munk, M. M. (1921), "The minimum induced drag of airfoils." National Advisory Committee for Aeronautics Tech. Rept121.

20) Tucker, V. A. (1987), "Gliding birds: the effect of variable wing span." J. exp. Biol, 133, 33–58.

21) Tucker, V. A.(1990), "Measuring aerodynamic interference drag between a bird body and the mounting strut of a drag balance." J. exp. Biol. 154, 439–461.

22) Tucker, V. A. (1992), "Pitching equilibrium, wing span and tail span in a gliding Harris' hawk, Parabuteo unicinctus." J. exp. Biol. 165, 21–41.

23) Tucker, V. A. and Heine, C. (1990), "Aerodynamics of gliding flight in a Harris' hawk, Parabuteo unicinctus." J. exp. Biol. 149, 469–489.

24) Tucker, V. A. and Parrott, G. C. (1970), "Aerodynamics of gliding flight in a falcon and other birds." J. exp. Biol. 52, 345–367.

25) Eastman N. Jacobs and Albert Sherman, "Wing-Fuselage interference comparison of conventional and aerofoil type fuselage combination." March 1937.

26) I. Kroo Stanford University, U.S.A. "Nonplanar wing concepts for increased aircraft efficiency" VKI lecture series on Innovative Configurations and Advanced Concepts for Future Civil Aircraft, June 6-10, 2005

27) Hahl, Robert W. (Falls Church, VA), "Lifting-fuselage/wing aircraft having low induced drag", United States Patent 5813628 (Source: http://www.freepatentsonline.com/5813628.html)

28) J. Reneaux, Onera, Applied Aerodynamics Department "Overview on drag reduction technologies for civil transport aircraft" European Congress on Computational Methods in Applied Sciences and Engineering (ECCOMAS) 2004.

29) Levy, H. and Riding, R.: "Burnelli's Lifting Fuselages." Aeroplane Monthly, Vol. 8, No. 3, March 1980, pp. 144-152.

30) Levy, H. and Riding, R.: "Burnelli's Lifting Fuselages." Aeroplane Monthly, Vol. 8, No. 5, April 1980, pp. 172-176.

31) Levy, H. and Riding, R.: "Burnelli's Lifting Fuselages." Aeroplane Monthly, Vol. 8, No. 6, May 1980, pp. 234-238.

32) Levy, H. and Riding, R.: "Burnelli's Lifting Fuselages." Aeroplane Monthly, Vol. 8, No. 7, July 1980, pp. 348-350.

33) Levy, H.: "Burnelli Lifting Fuselage Projects." Aeroplane Monthly, Vol. 8, No. 10, Oct. 1980, pp.516-517.

34) Wood, R. M. and Bauer, S. X. S.: "Flying Wings/Flying Fuselages." AIAA 2001-0311, Jan. 8-11, 2001.

35) Cantilli, E.: "Saga of the Lifting Body/Flying Wing." Flight, pp. 56-61, Fall 1996.

36) Mitchell, K. A.: "Burnelli and His Lifting-Body Transports." American Aviation Historical Society Journal, pp. 2-19, Spring 1997.

37) Mainuddin, Md., "Experimental Investigation of Lift to Drag Ratio Between Volumtrically Equivalent Fuselages" Thesis Publication, Department of Mechanical Engineering, BUET, Dhaka, March 2009.

38) Katz, J. and Byrne, S.: "Stall Resistance Features of Lifting-Body Airplane Configurations." AIAA 1998

39) Burnelli Monoplane. Aero Digest, Feb. 1929, pp. 94-96.

40) ttp://www.burnelli.com , November 2008

41) http: // www1.msfc.nasa.gov /Newsroom / news / releases / 2002/02-182.html, November 2002.

42) http://www.naa-usa.org/website/, November 2008

43) http://www.aerofiles.com, November 2008

44) Bushnell DM, Moore KJ. 1991. "Drag reduction in nature." Annu. Rev. Fluid Mech. 23:65- 79.

45) Yates JE, Donaldson CD. 1986. "A fundamental study of drag and an assessment of conventional drag-due-to-lift reduction devices." NASA CR 4004.

46) Spalart PR. 1998. "Airplane trailing vortices." Annu. Rev. Fluid Mech. 30:107-38.

47) Rokhsaz K. 1993. "A brief survey of wing tip devices for drag reduction." SAE 932574.

48) Munk M. 1981. "My early aerodynamic research – thoughts and memories." Annu. Rev. Fluid Mech. 13:1-7.

49) Kroo IM, Smith SC. 1990. "Computation of induced drag with nonplanar and deformed wakes." SAE 901933.

50) Whitcomb RT. 1994. "Research on methods for reducing the aerodynamic drag at transonic speeds." The Inaugural Eastman Jacobs Lecture, NASA Langley Research Center.

51) Lowson MV. 1990. "Minimum induced drag for wings with spanwise camber." AIAA J. Aircraft 27.\

52) Butler GF. 1982. "Effect of downwash of the induced drag of canard-wing combinations." AIAA J. Aircraft 19:410.

53) McGeer T, Kroo IM, 1983. "A fundamental comparison of canard and conventional configurations." AIAA J. of Aircraft.

54) Hackett JE. 1980. "Vortex drags reduction by aft-mounted diffusing vanes." ICAS Paper 80-13.4.

55) Rubbert PE. 1992. "Aircraft wingtip vorticity redistribution apparatus." United States Patent 5100085.

56) Patterson JC. 1985. "Wingtip vortex propeller." United States Patent 4533101.

57) La Roche U, Palffy S. 1996. "Wing-grid, a novel device for reduction of induced drag 20th wings." 20 ICAS Congress. Naples Italy. pg. 2303-9.

58) Hall KC, Hall SR. 1996. "Minimum induced power requirements for flapping flight." J. Fluid Mech. 323:285-315

59) De Young, J., "Induced Drag Ideal-Efficiency Factor of Arbitrary Lateral-Vertical Wing Forms," NASA CR-3357, Dec. 1980.

60) Smith, S.C., "A Computational and Experimental Study of Nonlinear Aspects of Induced Drag," Ph.D. Thesis, Stanford University, June 1995.

61) Van Dam, C.P., "Induced Drag Characteristics of Crescent-Moon-Shaped Wings," J. of Aircraft, Vol. 24, No.2, 1987.

62) Brayre, D.W., Walshe, D. E, and Germer, H. C., "Pressure Probe Selected for Three-Dimensional Flow Measuremnt", Rep. Memor, aero. Res. Cound. London, No. 3037, 1958.

63) Issac. W. Newton, "Experimental Study of Flow Separation on NACA 2412 by Flow Vsiualization", Virginia Poltechnic Institute, USA (Source: http://www.canyons.edu/departments/ENGINEERING/engr153notSoGoodReport.pdf)

64) Schmid, A. and Breitsamter C, "Experimental study on the Flowfield of a Delta-Canard-Configuration with Deflected Leading Edge", Springer Berlin / Heidelberg (ISSN1612-2909 (Print) 1060-0824 (Online))

65) Nay, Harvey O., "Low speed boundary layer and pressure distribution tests on a family of swept back wings", Engineer's Thesis, California Institute of Technology, USA

APPENDIX

(Separation Data Tables)

U∞ (km/hr)	0.25C			0.30C			0.375C			0.50C		
	y/C	U/U∞	θ (deg)	y/C	U/U∞	θ (deg)	y/C	U/U∞	θ (deg)	y/C	U/U∞	θ (deg)
30	0.005	-0.375	-9.21	0.005	-0.688	-82.43	0.005	-0.784	23.95	0.005	-0.635	-36.8
	0.0063	-0.375	-9.21	0.00563	-0.621	-38.74	0.0063	-0.772	23.95	0.0063	-0.635	-39.8
	0.0075	-0.35	-10.25	0.00625	-0.546	-24.68	0.0075	-0.761	23.95	0.0075	-0.607	-58.1
	0.0078	-0.132	-6.894	0.00688	-0.397	-17.84	0.0088	-0.725	23.95	0.0088	-0.562	-59.6
	0.0081	0.2962	-6.077	0.0075	0.1325	-11.79	0.01	-0.635	-52.04	0.01	-0.496	-67.2
	0.0084	0.4189	-4.897	0.00781	0.3244	-10.25	0.0113	-0.478	-24.18	0.0113	-0.35	-37.9
	0.0091	0.5923	-3.707	0.00844	0.513	-7.804	0.0131	0.4189	-11.51	0.0138	0.3746	-21.5
	0.0094	0.6623	-2.483	0.00875	0.5774	-7.207	0.0138	0.5298	-10.25	0.015	0.5298	-17.7
	0.01	0.7609	-2.106	0.00938	0.6882	-5.814	0.0144	0.6352	-8.939	0.0163	0.6489	-15.1
40	0.005	-0.011	-11.12	0.005	-0.516	206.3	0.005	-0.581	115.1	0.005	0.4496	-18.3
	0.0056	0.2306	-9.686	0.00563	-0.505	229.1	0.0056	-0.581	137.9	0.0056	0.4838	-18.4
	0.0058	0.3719	-7.905	0.00625	-0.419	-105.2	0.0063	-0.581	69.53	0.0063	0.5359	-17.8
	0.0059	0.4376	-7.397	0.00688	-0.301	-41.91	0.0069	-0.548	183.5	0.0069	0.5835	-16.5
	0.006	0.5157	-6.447	0.0075	-0.151	-24.25	0.0075	-0.495	-477.5	0.0075	0.6189	-15.4
	0.0061	0.5649	-5.827	0.00781	-0.086	-19.57	0.0081	-0.441	-121.9	0.0081	0.6684	-14.1
	0.0063	0.5925	-5.554	0.00813	0.1786	-15.36	0.0088	-0.366	-76.35	0.0088	0.6995	-13.8
	0.0064	0.6523	-4.548	0.00844	0.3262	-13.48	0.0094	-0.258	-41.18	0.0094	0.7293	-13.6
	0.0065	0.6842	-4.499	0.00875	0.4496	-11.39	0.01	-0.129	-28.16	0.01	0.7649	-12.5
	0.0069	0.7366	-3.695	0.00906	0.5458	-9.751	0.0106	0.1459	-19.89	0.0106	0.7855	-12.3
	0.0072	0.7855	-3.207	0.00938	0.6189	-8.808	0.0109	0.2729	-18.5	0.0113	0.8121	-12.1
	0.0075	0.8187	-2.757	0.00969	0.6763	-8.09	0.0113	0.3859	-15.61	0.0119	0.8379	-11.5

Table- 6.2.2: Separation data for the wing

U∞ (km/hr)	0.35C			0.40C			0.45C			0.50C		
	y/C	U/U∞	θ (deg)	y/C	U/U∞	θ (deg)	y/C	U/U∞	θ (deg)	y/C	U/U∞	θ (deg)
30	0.0017	-0.193	-21.64	0.00167	-0.193	-112.8	0.0017	-0.228	23.95	0.0017	-0.105	-44.44
	0.0019	-0.193	-21.64	0.00188	-0.175	-112.8	0.0021	-0.228	23.95	0.0021	-0.105	-44.44
	0.0021	-0.158	-14.05	0.00208	-0.175	-112.8	0.0025	-0.228	23.95	0.0025	-0.105	-44.44
	0.0023	-0.105	-12.53	0.00229	-0.14	-52.04	0.0029	-0.228	23.95	0.0029	-0.105	-44.44
	0.0025	-0.07	-13.35	0.0025	-0.105	-30.76	0.0033	-0.193		0.0038	-0.07	-67.23
	0.0027	-0.018	-9.487	0.00271	-0.053	-21.64	0.0038	-0.175		0.0042	-0.053	-90.03
	0.0029	0.2294	-8.618	0.00292	-0.018	-21.64	0.0042	-0.123	-52.04	0.0046	-0.018	-55.84
	0.0031	0.3244	-7.055	0.00313	0.1873	-15.13	0.0046	-0.07	-36.84	0.005	0.1325	-44.44
	0.0033	0.3974	-6.447	0.00333	0.2962	-13.6	0.005	0	-21.64	0.0054	0.2649	-31.77
	0.0035	0.4776	-5.973	0.00354	0.3746	-10.79	0.0054	0.2294	-21.64	0.0063	0.3974	-21.64
	0.0038	0.5461	-4.848	0.00375	0.4393	-10.25	0.0058	0.3746	-16.58	0.0067	0.4776	-19.24
40	0.0017	-0.076	-21.64	0.00167	-0.109	-11.87	0.0017	-0.239	8.749	0.0017	0.3612	-14.45
	0.0019	-0.022	-17.3	0.00188	-0.13	-10.25	0.0021	-0.228	23.95	0.0021	0.3901	-13.35
	0.0021	0.1806	-14.63	0.00208	-0.141	-12.53	0.0025	-0.207	69.53	0.0025	0.4299	-12.88
	0.0023	0.2949	-11.97	0.00229	-0.141	-12.53	0.0029	-0.185	206.3	0.0029	0.4663	-13.5
	0.0025	0.3759	-10.85	0.0025	-0.141	-12.53	0.0033	-0.141	-158.4	0.0038	0.5	-13.1
	0.0027	0.4423	-9.21	0.00292	-0.13	-11.12	0.0038	-0.087	-59.63	0.0042	0.5316	-12.78
	0.0029	0.5	-8.618	0.00333	-0.065	-11.51	0.004	-0.043	-39.88	0.0046	0.5614	-13.25
	0.0031	0.5517	-7.804	0.00354	0	-9.824	0.0042	-0.011	-31.41	0.005	0.5898	-12.75
	0.0033	0.6079	-6.447	0.00375	0.2331	-8.822	0.0044	0.2085	-24.04	0.0058	0.6427	-12.72
	0.0035	0.6511	-6.224	0.00396	0.3458	-7.189	0.0046	0.2949	-19.74	0.0067	0.6916	-12.7
	0.0038	0.6994	-5.626	0.00417	0.4423	-5.827	0.0048	0.3612	-18.39	0.0075	0.7445	-12.05

Table- 6.2.2: Separation data for the fuselage

APPENDIX- B

YAW METER

B.1 Measurement of flow direction with the help of three holes:

There are two common ways of measuring flow direction with the help of pressure probes; in either case the probes are similar and have a symmetric arrangement of sensing holes. In the first method, known as 'null-reading' or 'equi-balanced' method, the probe is oriented to a position at which same pressure is recorded in each hole; the flow direction can then be related to geometry of the probe. This relationship is easily established in the first instance by rotating the probe about its fore-and-lift axis through 180 degrees and realigning to give equal pressures; the true flow direction then lies at half the angle between the two probe positions. The second method is to keep the probe stationary and observe pressures or pressure differences whose relationship is obtained from calibration, which is done by orienting the probe in a steady known flow.

The first of these methods is recommended for two-dimensional flow and small flow angle. In investigations, where the flow is three dimensional and flow angle is large, the second method is adopted for measuring the flow angle.

Measurement of the flow direction by the second method is based on the fact that bthe fraction of total pressure of the flow field sensed by the pressure probes depends on the angle of incidence of the flow with the plane of the probe hole.

It is a maximum when the flow is normal to the plane of the probe hole and a minimum when parallel to it. Based on this philosophy, a multitude of probe with holes of different angles of inclination with flow direction is employed to measure the flow angle, which is called the yaw

meter. The sensitivity of the probe to "yaw" depends on the probes apex angle. In incompressible flow, the sensitivity of the yawmeter can be expressed as.

$$S(\Psi) = (P_1 - P_2) / [(H - P) \Psi] \qquad \dots \quad \dots \quad \dots \quad \dots \quad \dots \quad \dots \quad \dots \qquad (1)$$

where P_1 and P_2 are the pressure recorded in the tube. "H" is the total pressure recorded by the total head tube of the yaw meter, P is the atmospheric pressure and Ψ is the angle of the yaw meter, with respect to the flow direction. The magnitude of the pressure difference $\Delta P = P_1 - P_2$, which can be detected by the probe and the accuracy with which it can be measured, as these together determine the resolution attainable in the flow direction.

The smallest change of the flow angle which can be detected by a yaw meter system can be expressed by the equation,

$$\Delta \Psi = \Delta P_{min} / [S(\Psi) * \tfrac{1}{2} \rho V^2]$$

where ΔP_{min} is the minimum pressure difference that can be read on the manometer and $S(\Psi)$ is the yawmeter sensitivity [60].

In the present investigation, a multitube (3 tube) yawmeter made from stainless steel tube of 0.81 mm outside diameter and 0.5 mm inside diameter with the apex angle of 70^0 is used as shown in Figure B1. The Furness Control. pressure transducer used in the measurement could read pressure up to an accuracy .1 mm of water in the experimental range. Microsoft Excel Software is also used for data recording. The yaw meter in the present system, thus, could read up to an angle better than 0.02^0 at an air speed 10 m/s. This lower limit of resolution is adequate for present measurement.
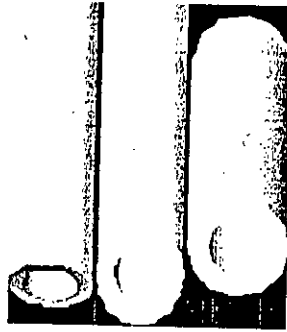
All tubes:

O.D. = 0.81 mm

I.D. = 0.40 mm

Figure-B1: 3D view of the yaw meter probes

B.2 Calibration of Yawmeter:

When a 3-tube yaw meter is placed in a flow field, the pressures recorded by different sensing tubes vary with varies with the flow direction. If P_1, P_2, and P_3 are the pressures recorded by the four compared tubes and the total head tube respectively (Figure B2), then the flow angle θ- (angle in the vertical x/y plane) can be found to be the function of ratio

$$(P_1 - P_2) \div (P_3 - (P_1 - P_3)/2)$$

During the process of calibration, the yawmeter is placed in the calibration rig at certain angle within $\pm 25^0$ with the flow direction. The velocity of the flow is maintained constant, yawmeter's angular position is varied.

For each angular position of the yawmeter, the pressure connections of the three tubes are selected with the help of a selector switch. The pressure ratio $(P_1 - P_2) \div (P_3 - (P_1 - P_3)/2)$ is plotted against angular position θ in Figure F3.

The calibration curve thus obtained shows a small deviation from the pastern equation (1). That the straight line did not pass through the origin but made a negative intercept on the vertical axis. This is attributed to the asymmetry of the placement of the compared tubes during fabrication.
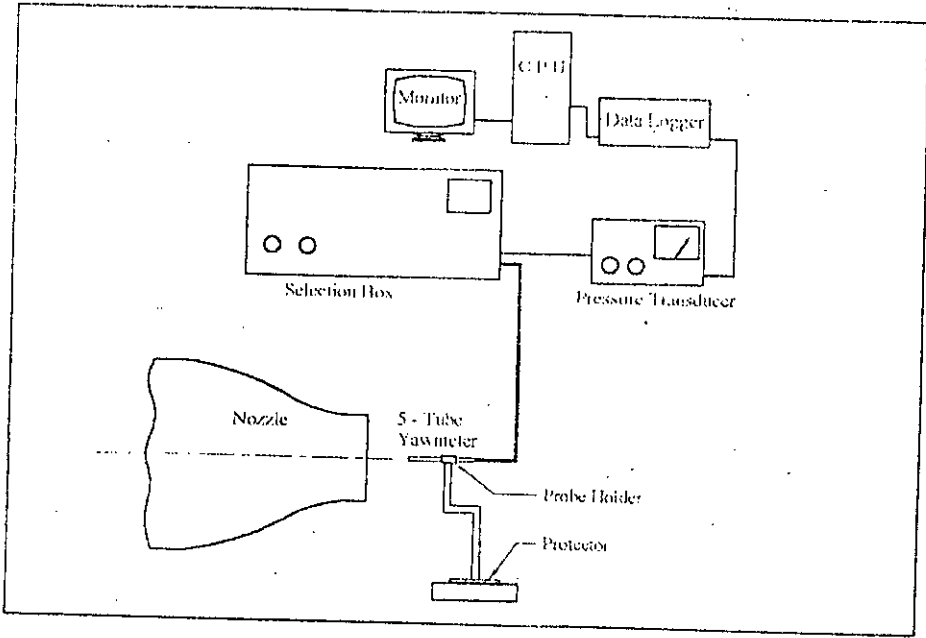
94

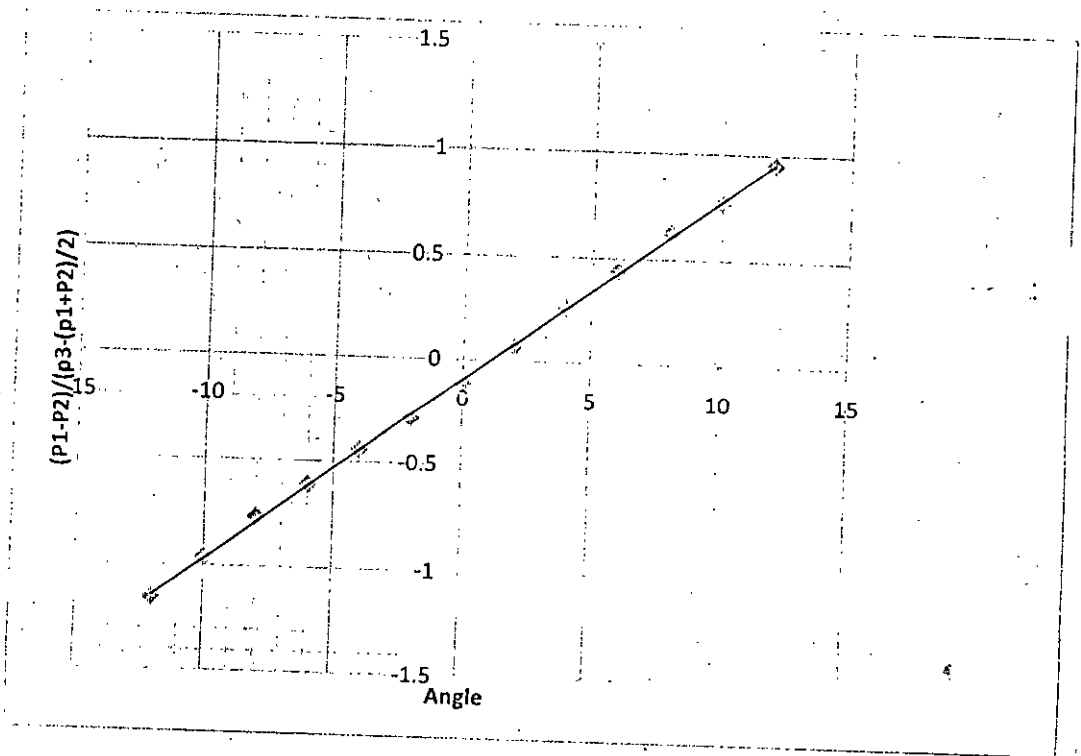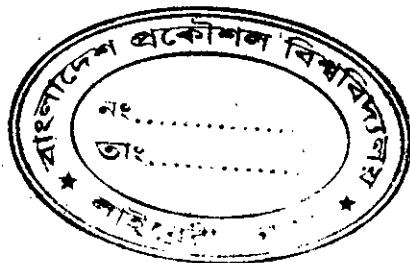**Figure- B2:** Calibration rig for three-tube yawmeter

Figure- B3: Calibration curve for the yawmeter

APPENDIX- C

Pressure transducer

Pressure transducers replace the conventional liquid column manometer used for pressure measurements. Pressure transducers convert the pressure into some equivalent electrical signals. Transducer's electronic circuits respond to pressure variations by the change of some resistance, capacitance or inductance, which is recorded in the form of voltage or current. The magnitude of the pressure is obtained from the calibrated pattern of the output signal of the transducer.

A pressure transducer basically consists of two closed chambers separated by common diaphragm. A pressure differential created between the chambers deflects the diaphragm. The deflection or strain thus produced is used to generate a suitable output signal.

In the electrical resistance type pressure transducer, a strain gage is fitted to the diaphragm to sense the pressure. The corresponding change in resistance in the gage due to the strain in the diaphragm is recorded by a galvanometer through the use of a wheat-stone type of bridge, which gives the information about the applied pressure.

A capacitance type pressure transducer, the deflection of the diaphragm is utilized to vary the volume of a closed space thereby to cause the change of capacitance in a circuit. The capacitor's response is picked up by a suitable output device via a suitable bridge circuit, giving a measure of the pressure.

The inductance type pressure transducer consists of a primary coil, magnetic core and a secondary coil. An alternating input voltage is impressed upon in the primary coil. The output voltage of the secondary coil depends on the inductive coupling between the core ends the coils, which is, in turn dependent on the relative position of the coils. Thus, the output voltage gives an indication of the pressure applied at the diaphragm.

Capacitance type pressure transducer is used in the present experiments, in which the output signal is obtained on a voltmeter dial graduated directly in mm of water. There are five different ranges of the scale. (10, 30, 100, 300 and 1000 mm) and the output voltage is to vary linearly with pressure, the magnitude being 1.0 volt for full scale deflections in all ranges.